

Fault-Tolerant Control for Multirotor Aerial Transportation Systems With Blade Damage

Hai Yu , Graduate Student Member, IEEE, Shizhen Wu , Graduate Student Member, IEEE, Wei He , Xiao Liang , Member, IEEE, Jianda Han , Member, IEEE, and Yongchun Fang , Senior Member, IEEE

Abstract—Aerial transportation systems are important ways for cargo delivery, especially in forest fire-fighting, postdisaster rescue, etc. While the harsh working environments may lead to multirotor failure, such as blade damage. Due to the inherent dynamic coupling existing between the payload and the multirotor, the blade damage will not only affect the dynamics of the multirotor and cause positioning failure but also aggravate the payload sway motion. In order to ensure the positioning accuracy and reduce payload oscillations, a fault-tolerant control scheme for the aerial transportation system is in urgent need. To this end, a finite-time disturbance observer-based nonlinear hierarchical control scheme is designed for the aerial transportation system to handle the lumped disturbance caused by blade damage. Specifically, the following two control objectives are achieved: 1) both the positioning of the multirotor and 2) the swing suppression of the payload with blade damage condition. Lyapunov techniques and LaSalle's invariance theorem are utilized to prove the convergence of the equilibrium point. Finally, simulation and experiment tests are conducted to verify the excellent performance of the proposed control scheme with different damage degrees of blades. As far as we know, this article proposes the first fault-tolerant controller for multirotor aerial transportation systems to realize simultaneous multirotor positioning and payload swing suppression even with blade damage.

Index Terms—Aerial transportation systems, antiswing, blade damage, fault-tolerant control.

I. INTRODUCTION

OVER the past decades, robots have been rapidly applied to various fields [1], [2], [3], including medical industry,

Manuscript received 24 July 2023; revised 8 October 2023 and 16 November 2023; accepted 9 December 2023. Date of publication 17 January 2024; date of current version 19 June 2024. This work was supported in part by the National Natural Science Foundation of China under Grant 62273187, Grant 62233011, and Grant 91848203, in part by the Young Elite Scientists Sponsorship Program by Tianjin under Grant TJSQNTJ-2020-21, and in part by the Haihe Lab of ITAI under Grant 22HHXCJC00003. (Corresponding author: Xiao Liang.)

The authors are with the Institute of Robotics and Automatic Information System, College of Artificial Intelligence, Nankai University, Tianjin 300350, China, and also with the Tianjin Key Laboratory of Intelligent Robotics, Nankai University, Tianjin 300350, China (e-mail: yuhai@mail.nankai.edu.cn; szwu@mail.nankai.edu.cn; howei@mail.nankai.edu.cn; liangx@nankai.edu.cn; hanjianda@nankai.edu.cn; fangyc@nankai.edu.cn).

This article has supplementary material provided by the authors and color versions of one or more figures available at <https://doi.org/10.1109/TIE.2023.3347848>.

Digital Object Identifier 10.1109/TIE.2023.3347848

agriculture, transportation, etc. Intelligent transportation systems employing ground vehicles [4], vessels [5], and aerial vehicles [6] have improved the transportation efficiency and promoted the transportation industry. Particularly, for aerial transportation systems, multirotor unmanned aerial vehicles (UAVs) play an important role due to their vertical takeoff and landing ability, hovering capability, excellent maneuverability, and high flexibility.

Recently, cable-suspended aerial transportation systems have been extensively studied [7], [8], [9], [10]. Based on the robust integral of the sign of the error (RISE), a nonlinear control law [7] is designed to implement multirotor trajectory tracking and payload swing elimination under unknown turbulence. To pass through windows and avoid obstacles, an aggressive payload position and swing angle trajectory generation approach [8] is designed by imposing payload acceleration limitations. Without any time-scale separation, a path-following controller is devised through the monolithic design approach [9], which can guarantee that the payload converges to a given path and attains path invariance. Aiming at constraining the position of the multirotor, an adaptive control method is designed in [10] to effectively reduce the multirotor positioning overshoots and suppress the payload swing. However, the smooth application of the aforementioned methods usually needs to ensure that the aerial transportation system is free from any failure or damage, while aerial transportation systems are extensively employed in such complex and dangerous scenarios as forest fire-fighting, material delivery, post-disaster rescue. Specifically, in the execution of the mission, multirotors may collide with trees, walls, or other flying objects, leading to blade damage. Besides, the swing of the payload will increase due to the collision, which will further put the transportation system in a risky state. Therefore, it is of great importance for aerial transportation systems to deal with such emergencies and ensure the safety of the payload.

Plenty of studies have been investigated to deal with multirotor UAV failures over the last decade. In general, there are mainly two types of fault-tolerant control (FTC) schemes [11], passive FTC, and active FTC. Passive FTC [12], [13], [14], is designed to be robust against a class of presumed faults without the requirement of fault detection and diagnosis. In [12], a nonlinear robust adaptive fault-tolerant altitude and attitude tracking scheme is proposed to accommodate the actuators' partial fault. To ensure fixed time estimation and finite-time adaptation of actuator faults, a backstepping integral nonsingular fast terminal sliding mode controller is designed in [13], which

has the ability to accommodate faults quickly without loss of performance. An adaptive neural network FTC scheme is developed in [14], which can handle nonparametric uncertainties and be tolerant to unexpected actuation faults. Unlike passive FTC, active FTC [15], [16], [17], [18], [19], [20], is designed based on control signals reconfiguration with a fault diagnosis scheme to detect and identify the system's faults. In [15], a fault-free control scheme and a nonsingular terminal sliding mode control method are switched through fault detection and isolation method to accommodate a complete rotor failure. To minimize accidents from failures, Chung et al. [16] propose an optimal control to reconfigure the multirotor thrust, which maintains the controllability of altitude when the control output cannot compensate for faults because of the motor saturation. In [17], an adaptive sliding mode control scheme is presented to handle several actuators' control effectiveness loss with model uncertainties, whose experimental results show the superiority in fault-tolerant controller compared with the model-based fault estimator and the conventional adaptive sliding mode control strategy. Ke et al. [18] design a uniform fault-tolerant controller, which does not require controller switching when a motor completely fails. By employing the broad learning system approximation technique, a distributed fault-tolerant tracking control algorithm is designed for the UAV formation systems to identify the unknown lumped disturbances caused by actuator faults and input constraints in [19]. To compensate for the changes in multirotor dynamics due to motor faults and ensure flight safety, a nonlinear observer is utilized in the sliding mode control method to estimate the effect of motor faults [20]. Noteworthy, despite the above researches have been carried out on the FTC of multirotor UAV, it is difficult to extend these methods to the aerial transportation systems due to the dynamic coupling caused by payload swing. Compared to a single multirotor, the aerial transportation system presents much more complex underactuated characteristics due to the system's degrees of freedom changing from six to eight, while the control inputs remain unchanged at four, which makes the control problem much more difficult. Besides, the payload oscillation increases the dynamic coupling and nonlinearity, and the blade damage will not only affect the dynamics of the multirotor but also indirectly affect the motion of the payload, causing unpredictable payload vibration, which makes the precise control more challenging.

In this article, a hierarchical control scheme is designed for aerial transportation systems based on the finite-time disturbance observer (FTDO), which is employed to compensate for the loss of the multirotor force and torque caused by blade damage. Specifically, an enhanced-coupling signal containing both the payload swing angle and multirotor position is utilized to construct the outer loop controller, while the inner loop controller is designed on the basis of the geometric control scheme. Subsequently, the stability of the closed-loop system is guaranteed by Lyapunov techniques and LaSalle's invariance theorem, together with the theory of cascading systems. Finally, the performance of the proposed control law is verified by several convincing experimental tests with cut blades. The major merits of the proposed control scheme are summarized as follows.

- 1) Existing researches only study the FTC of the multirotor [12], [13], [14], [15], [16], [17], [18], [19], [20]; however, due to the introduction of the payload, the aerial transportation system has more complex dynamic coupling existing between the payload motion and the multirotor. The blade damage will not only affect the dynamics of the multirotor but also indirectly affect the motion of the payload, causing unpredictable payload vibration. Besides, the payload oscillation will also pose challenges to the FTC of the multirotor with blade damage, which makes precise control much more difficult. This article overcomes the above problem and presents the first fault-tolerant control scheme for the aerial transportation system to tolerate blade damage.
- 2) In fact, it is difficult to directly design an observer to estimate the disturbance of the aerial transportation system due to the underactuated characteristics. In this article, by introducing a well designed virtual signal, the complex outer loop subsystem dynamic model is first transformed, based on which, the finite-time disturbance observer can be conveniently applied to the system. Thus, the lumped disturbance caused by the blade damage can be unbiased estimated in finite-time theoretically, which brings great convenience to the subsequent controller design.
- 3) Inspired by the payload position, an enhanced-coupling error signal incorporating information on both multirotor's and payload's motion is constructed for the controller design. Since the payload swing angle signals are injected into the control scheme, the state coupling between the multirotor and the payload is increased. By utilizing the enhanced-coupling signal, the control scheme not only takes a concise form but also greatly improves the transient performance in payload swing suppression. As presented in the simulation and experimental results, the proposed control method can effectively guarantee the multirotor positioning as well as the payload swing elimination simultaneously.

The rest of this article is organized as follows. The control problem for the aerial transportation system with blade damage is formulated in Section II. Section III provides the disturbance estimation, controller design and stability analysis. Subsequently, in Section IV, two groups of experimental results are provided to show the performance of the proposed control scheme. Finally, Section V concludes this article.

Notation: Throughout this article, C_* and S_* denote the abbreviations of $\cos(\theta_*)$ and $\sin(\theta_*)$, respectively. $\text{sk}(\cdot) : \mathbb{R}^3 \rightarrow \mathfrak{so}(3)$ is defined by the relation that $\text{sk}(\mathbf{x})\mathbf{y} = \mathbf{x} \times \mathbf{y}$ for all $\mathbf{x}, \mathbf{y} \in \mathbb{R}^3$. $\text{vex}(\cdot) : \mathfrak{so}(3) \rightarrow \mathbb{R}^3$ is the inverse operation of $\text{sk}(\cdot)$. For a vector $\mathbf{h} \in \mathbb{R}^n$, define $\mathbf{h}^{[p]} = [\text{sgn}(h_1)|h_1|^p, \dots, \text{sgn}(h_n)|h_n|^p]^\top$, $\text{sgn}(\mathbf{h}) = [\text{sgn}(h_1), \dots, \text{sgn}(h_n)]^\top$, $|\mathbf{h}| = [|h_1|, \dots, |h_n|]^\top$, $\text{Cosh}(\mathbf{h}) = [\cosh(h_1), \dots, \cosh(h_n)]^\top$, $\text{Tanh}(\mathbf{h}) = [\tanh(h_1), \dots, \tanh(h_n)]^\top$, $\text{Ln}(\mathbf{h}) = [\ln(h_1), \dots, \ln(h_n)]^\top$, and $\text{diag}(\mathbf{h})$ is a diagonal matrix with diagonal elements of h_1, \dots, h_n . $\lambda_M(\star)$ and $\lambda_m(\star)$ denote the maximum eigenvalue and minimum eigenvalue of matrix \star , respectively.

TABLE I
SYMBOLS AND DEFINITIONS OF THE SYSTEM

Symbol	Definition
$M, m \in \mathbb{R}$	Mass of multirotor and payload
$g \in \mathbb{R}$	Gravitational acceleration
$l \in \mathbb{R}$	Cable length
$J = \text{diag}([J_1, J_2, J_3]) \in \mathbb{R}^{3 \times 3}$	Multirotor's moment of inertia
$R \in SO(3)$	Rotation matrix from $\{\mathcal{B}\}$ to $\{\mathcal{T}\}$
$Re_3 = [R_{13}, R_{23}, R_{33}]^T$	Last column of rotation matrix R
$\gamma = [x, y, z]^T \in \mathbb{R}^3$	Multirotor position
$\Theta = [\theta_x, \theta_y]^T \in \mathbb{R}^2$	Payload swing angle
$\gamma_p = [x_p, y_p, z_p]^T \in \mathbb{R}^3$	Payload position
$q = [\gamma^T, \Theta^T]^T \in \mathbb{R}^5$	Generalized coordinate of outer loop subsystem
$\Omega = [\Omega_1, \Omega_2, \Omega_3]^T \in \mathbb{R}^3$	Angular velocity of multirotor in frame $\{\mathcal{B}\}$
$\gamma_d = [x_d, y_d, z_d]^T \in \mathbb{R}^3$	Desired multirotor position
$q_d = [\gamma_d^T, 0, 0]^T \in \mathbb{R}^5$	Desired outer loop state
$R_d \in SO(3)$	Desired rotation matrix
$\Omega_d \in \mathbb{R}^3$	Desired angular velocity
$M_c(q) \in \mathbb{R}^{5 \times 5}$	Inertia matrix
$V_c(q, \dot{q}) \in \mathbb{R}^{5 \times 5}$	Centripetal–Coriolis matrix
$G(q) \in \mathbb{R}^5$	Gravity vector
$u = [fRe_3, 0, 0]^T \in \mathbb{R}^5$	Outer loop control input vector
$F_{qdis} = [d_x, d_y, d_z, 0, 0]^T \in \mathbb{R}^5$	Outer loop disturbance
$f \in \mathbb{R}$	Applied thrust generated by multirotor
$\tau = [\tau_1, \tau_2, \tau_3]^T \in \mathbb{R}^3$	Torque generated by multirotor
$\tau_{dis} = [d_{\Omega_1}, d_{\Omega_2}, d_{\Omega_3}]^T \in \mathbb{R}^3$	Inner loop disturbance
$e_3 = [0, 0, 1]^T$	Unit vector

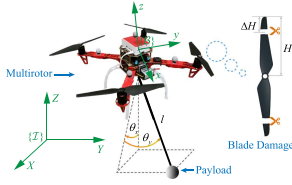


Fig. 1. Aerial transportation system with blade damage.

II. PROBLEM FORMULATION

The schematic diagram of the aerial transportation system with blade damage is depicted by Fig. 1, where $\{\mathcal{T}\}$ represents the right-hand inertia frame, $\{\mathcal{B}\}$ is the body-fixed frame. The symbols and definitions are listed in Table I. For practical conditions, the following reasonable assumptions of the aerial transportation system are widely made [7], [10], [21], [22].

Assumption 1: The payload is always beneath the multirotor, i.e., $-\pi/2 < \theta_x(t), \theta_y(t) < \pi/2, \forall t \geq 0$.

Assumption 2: The suspension cable is massless and always taut.

A. Dynamic Modeling

The dynamic model can be divided into two subsystems as follows: 1) the inner loop subsystem is the rotation of the multirotor, and 2) the outer loop subsystem is composed of the multirotor translation and payload motion. Specifically, the loss of the control input caused by the blade damage is established as uncertainties added on the system. According to the geometric relationship in Fig. 1, the payload's position can be expressed as $\gamma_p(t) = [x + lS_xC_y, y + lS_y, z - lC_xC_y]^T$, where C_x, C_y, S_x, S_y are the abbreviations of $\cos(\theta_x), \cos(\theta_y), \sin(\theta_x), \sin(\theta_y)$. The

Lagrangian of the outer loop subsystem is expressed as $L_{ou} = \frac{1}{2}M\dot{\gamma}^T\dot{\gamma} + \frac{1}{2}m\dot{\gamma}_p^T\dot{\gamma}_p - (Mgz + mgz_p)$. The generalized force can be calculated by $Q_i = \delta W / \delta q_i, i = \{1, \dots, 5\}$, where δq_i is the virtual displacement and $\delta W = (fRe_3 + [d_x, d_y, d_z]^T) \cdot \delta\gamma$ is the virtual work. Finally, based on the Lagrange's equation $\frac{d}{dt} \frac{\partial L_{ou}}{\partial \dot{q}_i} - \frac{\partial L_{ou}}{\partial q_i} = Q_i, i = \{1, \dots, 5\}$, the outer loop dynamic model can be established as

$$M_c(q)\ddot{q} + V_c(q, \dot{q})\dot{q} + G(q) = u + F_{qdis}. \quad (1)$$

For the inner loop subsystem, since the cable is suspended on the multirotor's center of mass, the rotational dynamics is not influenced by the payload. Thus, the inner loop subsystem stays the same as the situation without suspended payload [10], [23], which is represented as

$$\dot{R} = Rsk(\Omega) \quad (2)$$

$$J\dot{\Omega} + sk(\Omega)J\Omega = \tau + \tau_{dis}. \quad (3)$$

To facilitate subsequent analysis, the outer loop dynamic model (1) can be expanded as follows [10], [24], [25], [26]:

$$(M + m)\ddot{x} + ml \left(\ddot{\theta}_x C_x C_y - \ddot{\theta}_y S_x S_y - \dot{\theta}_x^2 S_x C_y - \dot{\theta}_y^2 S_x C_y - 2\dot{\theta}_x \dot{\theta}_y C_x S_y \right) = fR_{13} + d_x \quad (4)$$

$$(M + m)\ddot{y} + ml \left(\ddot{\theta}_y C_y - \dot{\theta}_y^2 S_y \right) = fR_{23} + d_y \quad (5)$$

$$(M + m)\ddot{z} + ml \left(\ddot{\theta}_x S_x C_y + \ddot{\theta}_y C_x S_y + \dot{\theta}_x^2 C_x C_y + \dot{\theta}_y^2 C_x C_y - 2\dot{\theta}_x \dot{\theta}_y S_x S_y \right) = fR_{33} - (M + m)g + d_z \quad (6)$$

$$ml\ddot{x}C_xC_y + ml\ddot{z}S_xC_y + ml^2\ddot{\theta}_xC_y^2 - 2ml^2\dot{\theta}_x\dot{\theta}_yC_yS_y$$

$$+ mglS_x C_y = 0 \quad (7)$$

$$\begin{aligned} & - ml\ddot{x}_x S_x S_y + ml\ddot{y}C_y + ml\ddot{z}C_x S_y + ml^2\ddot{\theta}_y + ml^2\dot{\theta}_x^2 C_y S_y \\ & + mglC_x S_y = 0. \end{aligned} \quad (8)$$

Similar to many Euler–Lagrange systems [10], [21], [22], it is not difficult to obtain that dynamic model (1) satisfies the following property:

Property 1: M_c and V_c satisfy the skew-symmetric relationship, i.e., $\boldsymbol{\eta}^\top (\frac{1}{2}\dot{M}_c - V_c)\boldsymbol{\eta} = 0, \forall \boldsymbol{\eta} \in \mathbb{R}^5$.

Remark 1: Similar to many cable-suspended systems such as cranes and aerial transportation systems [7], [8], [9], [10], [21], [22], this article focuses on the situation that the cable is rigid. However, when the platform or payload is in unexpected motion, the suspension cable may be slack. In this case, the system dynamic model will be established as a differentially flat hybrid system. In future studies, more applicable fault-tolerant control algorithms will be designed for the aerial transportation system with the consideration of the slack cable.

Remark 2: Based on the blade-element theory [27], the impact of the blade damage is first analyzed. The chord length and setting angle of the blade-element are assumed to be invariable along span direction, and one propeller has two blades. The relationship between the i th propeller thrust f_i and rotation speed v_i (rad/s) can be presented as

$$f_i = 2 \int_0^H \frac{1}{2} \rho (2\pi v_i r)^2 C_L b dr = v_i^2 \rho (2\pi)^2 C_L b \int_0^H r^2 dr = v_i^2 c_T$$

where ρ is the air density, C_L is the lift coefficient, b denotes the chord length of the blade, H represents the propeller radius, and $c_T = \rho(2\pi)^2 C_L b \int_0^H r^2 dr$. The torque of the propeller against the body can be expressed as

$$\tau_{zi} = 2 \int_0^H \frac{1}{2} \rho (2\pi v_i r)^2 C_D b r dr = v_i^2 \rho (2\pi)^2 C_D b \int_0^H r^3 dr = v_i^2 c_{\tau}$$

where C_D is the drag coefficient, and $c_{\tau} = \rho(2\pi)^2 C_D b \int_0^H r^3 dr$. As presented in Fig. 1, at the same motor speed, when the blade radius reduce ΔH , the coefficient of the propeller thrust loss ζ_{f_i} and torque loss $\zeta_{\tau_{zi}}$ are

$$\begin{aligned} \zeta_{f_i} &= \frac{v_i^2 \rho (2\pi)^2 C_L b \int_0^{H-\Delta H} r^2 dr}{v_i^2 \rho (2\pi)^2 C_L b \int_0^H r^2 dr} = \frac{(H - \Delta H)^3}{H^3} \\ \zeta_{\tau_{zi}} &= \frac{v_i^2 \rho (2\pi)^2 C_D b \int_0^{H-\Delta H} r^3 dr}{v_i^2 \rho (2\pi)^2 C_D b \int_0^H r^3 dr} = \frac{(H - \Delta H)^4}{H^4}. \end{aligned}$$

Taking the X-shaped quadrotor as an example, the relation between the motor rotation speed and control inputs can be expressed as

$$\begin{bmatrix} f \\ \tau_1 \\ \tau_2 \\ \tau_3 \end{bmatrix} = \begin{bmatrix} \zeta_{f_1} c_T & \zeta_{f_2} c_T & \zeta_{f_3} c_T & \zeta_{f_4} c_T \\ \frac{\sqrt{2}}{2} d \zeta_{f_1} c_T & -\frac{\sqrt{2}}{2} d \zeta_{f_2} c_T & -\frac{\sqrt{2}}{2} d \zeta_{f_3} c_T & \frac{\sqrt{2}}{2} d \zeta_{f_4} c_T \\ \frac{\sqrt{2}}{2} d \zeta_{f_1} c_T & \frac{\sqrt{2}}{2} d \zeta_{f_2} c_T & -\frac{\sqrt{2}}{2} d \zeta_{f_3} c_T & -\frac{\sqrt{2}}{2} d \zeta_{f_4} c_T \\ \zeta_{\tau_{z1}} c_{\tau} & -\zeta_{\tau_{z2}} c_{\tau} & \zeta_{\tau_{z3}} c_{\tau} & -\zeta_{\tau_{z4}} c_{\tau} \end{bmatrix} \begin{bmatrix} v_1^2 \\ v_2^2 \\ v_3^2 \\ v_4^2 \end{bmatrix}$$

where d stands for the half of motor-to-motor distance, $\zeta_{f_i} c_T$ and $\zeta_{\tau_{zi}} c_{\tau}, i = 1, 2, 3, 4$ are the mapping coefficients affected

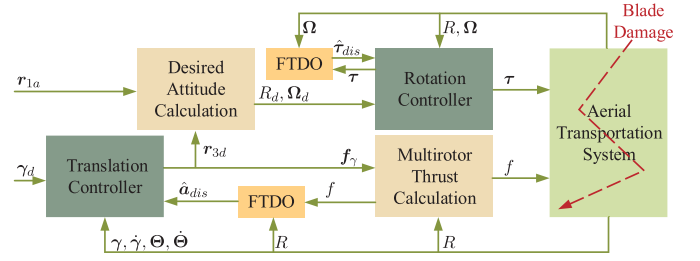


Fig. 2. Diagram of the proposed control algorithm.

by blade damage, which are different from the original mapping coefficients. The reduction of the mapping coefficients results in the loss of force and torque of the quadrotor, which can be regarded as lumped disturbances added to the system. Similar to [20], [28], [29], and [30], treating faults as disturbances is a common method in fault-tolerant control.

Based on the analysis in Remark 2, and similar to many recent publications [20], [28], [29], [30], [31], the following assumptions are made.

Assumption 3: The lumped disturbance caused by the blade damage is bounded.

Assumption 4: The derivative of the disturbance \dot{d}_k is bounded and satisfies $|\dot{d}_k| \leq D_k$, where D_k is the constant, for $k = x, y, z, \Omega_1, \Omega_2, \Omega_3$.

Remark 3: Compared with the dynamics of the single multirotor, whose outer loop subsystem takes the following form:

$$M\dot{\gamma} = fRe_3 - Mge_3 + [d_x, d_y, d_z]^\top$$

the cable-suspended aerial transportation system presents a more complicated outer loop dynamics due to the coupling between the multirotor position and the payload swing angle as given in (4)–(8). It is worth noting that the increased payload swing dynamics cannot be directly controlled, so the outer loop subsystem of the aerial transportation system is underactuated, which is more complex than the dynamics of the outer loop subsystem of a single multirotor.

B. Control Objective

The multirotor position error is defined as $e_\gamma = \gamma - \gamma_d$, thus, the outer loop state error can be defined as $e_q = [e_\gamma^\top, \Theta^\top]^\top \in \mathbb{R}^5$. The multirotor's attitude and angular velocity tracking errors [32] are defined as $e_R = \frac{1}{2} \text{vex}(R_d^\top R - R^\top R_d), e_\Omega = \Omega - R^\top R_d \Omega_d$. The control objective is to drive the multirotor from its initial position to the constant desired one γ_d , while eliminating the payload swing even with blade damage, i.e.,

$$e_\gamma \rightarrow \mathbf{0}_{3 \times 1}, \Theta \rightarrow \mathbf{0}_{2 \times 1}, e_q \rightarrow \mathbf{0}_{5 \times 1}, e_R \rightarrow \mathbf{0}_{3 \times 1}, e_\Omega \rightarrow \mathbf{0}_{3 \times 1}.$$

The control structure is presented as shown in Fig. 2.

III. DISTURBANCE PROCESSING AND CONTROLLER DESIGN

A. Disturbance Observer

For the convenience of subsequent analysis, a virtual signal

$$\chi = \left[x + \frac{m}{M+m} l S_x C_y, y + \frac{m}{M+m} l S_y, \right. \\ \left. z + \frac{m}{M+m} l (1 - C_x C_y) \right]^\top$$

is elaborately constructed for the outer loop subsystem, thus, models (4)–(6) can be transformed into the following form:

$$\ddot{\chi} = \mathbf{a}_\chi + \mathbf{a}_{\text{dis}}$$

where $\mathbf{a}_\chi = \frac{1}{M+m} f R e_3 - g e_3$ and $\mathbf{a}_{\text{dis}} = \frac{1}{M+m} [d_x, d_y, d_z]^\top$.

Subsequently, define auxiliary variables $e_\chi = \dot{\chi} - \delta_\chi$, $e_\omega = \Omega - \delta_\omega$, where δ_χ and δ_ω are obtained by integrating the following equations:

$$\dot{\delta}_\chi = \mathbf{a}_\chi + c_{\alpha_\chi} e_\chi^{[\alpha_\chi]} + c_{\beta_\chi} e_\chi^{[\beta_\chi]} + \xi_\chi \quad (9)$$

$$\dot{\delta}_\omega = J^{-1} (\tau - \text{sk}(\Omega) J \Omega) + c_{\alpha_\omega} e_\omega^{[\alpha_\omega]} + c_{\beta_\omega} e_\omega^{[\beta_\omega]} + \xi_\omega \quad (10)$$

the coefficients matrices $c_{\alpha_\chi}, c_{\beta_\chi}, c_{\alpha_\omega}, c_{\beta_\omega} \in \mathbb{R}_+^{3 \times 3}$ are positive definite diagonal matrices, $0 < \alpha_\chi, \alpha_\omega < 1, \beta_\chi, \beta_\omega > 1$ are positive parameters, ξ_χ and ξ_ω are intermediate variables to be constructed. Then, define the sliding surface as

$$s_\chi = \dot{e}_\chi + c_{\alpha_\chi} e_\chi^{[\alpha_\chi]} + c_{\beta_\chi} e_\chi^{[\beta_\chi]} \quad (11)$$

$$s_\omega = \dot{e}_\omega + c_{\alpha_\omega} e_\omega^{[\alpha_\omega]} + c_{\beta_\omega} e_\omega^{[\beta_\omega]} \quad (12)$$

and the disturbance observer of \mathbf{a}_{dis} and τ_{dis} are designed as

$$\hat{\mathbf{a}}_{\text{dis}} = \xi_\chi \quad (13)$$

$$\dot{\xi}_\chi = (\eta_{d_\chi} + \kappa_{d_\chi}) \text{sgn}(s_\chi), \xi_\chi(0) = \mathbf{0}_{3 \times 1} \quad (14)$$

$$\hat{\tau}_{\text{dis}} = J \xi_\omega \quad (15)$$

$$\dot{\xi}_\omega = (\eta_{d_\omega} + \kappa_{d_\omega}) \text{sgn}(s_\omega), \xi_\omega(0) = \mathbf{0}_{3 \times 1} \quad (16)$$

where $\eta_{d_\chi}, \kappa_{d_\chi}, \eta_{d_\omega}, \kappa_{d_\omega} \in \mathbb{R}_+^{3 \times 3}$ are positive definite diagonal matrices. The specific forms are

$$\eta_{d_\chi} = \text{diag}([\eta_{d_x}, \eta_{d_y}, \eta_{d_z}]), \eta_{d_\omega} = \text{diag}([\eta_{d_{\omega_1}}, \eta_{d_{\omega_2}}, \eta_{d_{\omega_3}}])$$

$$\kappa_{d_\chi} = \text{diag}([\kappa_{d_x}, \kappa_{d_y}, \kappa_{d_z}]), \kappa_{d_\omega} = \text{diag}([\kappa_{d_{\omega_1}}, \kappa_{d_{\omega_2}}, \kappa_{d_{\omega_3}}])$$

wherein κ_{di} satisfies $\kappa_{di} > \frac{1}{M+m} D_i$, for $i = x, y, z$ and $\kappa_{d\omega_j}$ satisfies $\kappa_{d\omega_j} > D_{\Omega_j}$, for $j = 1, 2, 3$.

Lemma 1: Consider the following scalar system [33], [34], [35]:

$$\dot{\nu} = -c_\alpha \text{sgn}(\nu) |\nu|^\alpha - c_\beta \text{sgn}(\nu) |\nu|^\beta, \quad \nu(0) = \nu_0$$

where c_α, c_β are positive constants, $0 < \alpha < 1$ and $\beta > 1$. The equilibrium point of the above system is finite-time stable and its settling time is bounded by: $T < T_{\text{max}} = \frac{1}{c_\alpha} \frac{1}{1-\alpha} + \frac{1}{c_\beta} \frac{1}{\beta-1}$.

Theorem 1: The disturbance observer (13)–(16) guarantees that the disturbance estimation error of \mathbf{a}_{dis} and τ_{dis} converge to zero in finite-time, under Assumption 4 and the conditions

$$0 < \alpha_\chi, \alpha_\omega < 1, \beta_\chi, \beta_\omega > 1, \kappa_{di} > \frac{1}{M+m} D_i, \kappa_{d\omega_j} > J_j^{-1} D_{\Omega_j}$$

for $i = x, y, z$ and $j = 1, 2, 3$.

Proof: The time derivative of e_χ and e_ω with respect to time are derived as follows:

$$\dot{e}_\chi = \ddot{\chi} - \dot{\delta}_\chi = \mathbf{a}_{\text{dis}} - c_{\alpha_\chi} e_\chi^{[\alpha_\chi]} - c_{\beta_\chi} e_\chi^{[\beta_\chi]} - \xi_\chi \quad (17)$$

$$\dot{e}_\omega = \dot{\Omega} - \dot{\delta}_\omega = J^{-1} \tau_{\text{dis}} - c_{\alpha_\omega} e_\omega^{[\alpha_\omega]} - c_{\beta_\omega} e_\omega^{[\beta_\omega]} - \xi_\omega. \quad (18)$$

Then, comparing (17) and (18) with (11) and (12), one can obtain that $s_\chi = \mathbf{a}_{\text{dis}} - \xi_\chi$, $s_\omega = J^{-1} \tau_{\text{dis}} - \xi_\omega$. Substituting (14) and (16) into the time derivative of the sliding surface s_χ and s_ω leads to

$$\dot{s}_\chi = \dot{\mathbf{a}}_{\text{dis}} - \dot{\xi}_\chi = \dot{\mathbf{a}}_{\text{dis}} - (\eta_{d_\chi} + \kappa_{d_\chi}) \text{sgn}(s_\chi) \quad (19)$$

$$\dot{s}_\omega = J^{-1} \dot{\tau}_{\text{dis}} - \dot{\xi}_\omega = J^{-1} \dot{\tau}_{\text{dis}} - (\eta_{d_\omega} + \kappa_{d_\omega}) \text{sgn}(s_\omega). \quad (20)$$

Subsequently, selecting a positive Lyapunov function candidate $V_{d_\chi} = \frac{1}{2} s_\chi^\top s_\chi$, and substituting (19) into the differentiation of V_{d_χ} , one has

$$\dot{V}_{d_\chi} = s_\chi^\top \dot{s}_\chi = s_\chi^\top (\dot{\mathbf{a}}_{\text{dis}} - (\eta_{d_\chi} + \kappa_{d_\chi}) \text{sgn}(s_\chi)) \\ \leq (|\dot{\mathbf{a}}_{\text{dis}}|^\top - [\kappa_{d_x}, \kappa_{d_y}, \kappa_{d_z}]) |s_\chi| - [\eta_{d_x}, \eta_{d_y}, \eta_{d_z}] |s_\chi| \\ \leq -[\eta_{d_x}, \eta_{d_y}, \eta_{d_z}] |s_\chi| \quad (21)$$

which indicates the sliding surface s_χ converge to zero in finite-time, i.e., $s_\chi = \mathbf{0}_{3 \times 1}$. Therefore, from (11), one achieves $\dot{e}_\chi = -c_{\alpha_\chi} e_\chi^{[\alpha_\chi]} - c_{\beta_\chi} e_\chi^{[\beta_\chi]}$. Based on Lemma 1, the equilibrium point of (17) is finite-time stable, i.e.,

$$\lim_{t \rightarrow t_{f_\chi}} e_\chi = \mathbf{0}_{3 \times 1} \quad (22)$$

where t_{f_χ} represents the finite convergence time. Define the estimation error of the disturbance \mathbf{a}_{dis} as $\tilde{\mathbf{a}}_{\text{dis}} = \mathbf{a}_{\text{dis}} - \hat{\mathbf{a}}_{\text{dis}}$, from (13) and (17)–(22), it is obvious that $\tilde{\mathbf{a}}_{\text{dis}}$ is bounded and

$$\lim_{t \rightarrow t_{f_\chi}} \tilde{\mathbf{a}}_{\text{dis}} = \mathbf{0}_{3 \times 1}. \quad (23)$$

In an analogous method, for the inner loop subsystem, select the positive Lyapunov function candidate as $V_{d_\omega} = \frac{1}{2} s_\omega^\top s_\omega$, and define the estimation error of the torque disturbance τ_{dis} as $\tilde{\tau}_{\text{dis}} = \tau_{\text{dis}} - \hat{\tau}_{\text{dis}}$. Taking the time derivative of V_{d_ω} , one can obtain that $\dot{V}_{d_\omega} \leq -[\eta_{d_{\omega_1}}, \eta_{d_{\omega_2}}, \eta_{d_{\omega_3}}] |s_\omega|$. Thus, $\tilde{\tau}_{\text{dis}}$ is bounded and $\lim_{t \rightarrow t_{f_\Omega}} \tilde{\tau}_{\text{dis}} = \mathbf{0}_{3 \times 1}$, where t_{f_Ω} represents the finite convergence time. In summary, Theorem 1 is proved. ■

B. Controller Design

To efficiently eliminate the payload swing, inspired by the payload position $\gamma_p = \gamma + [l S_x C_y, l S_y, -l C_x C_y]^\top$, a virtual desired multirotor position is constructed by introducing the swing angle information, taking the following form as

$$\Gamma_d = \gamma_d + \vartheta [S_x C_y, S_y, 1 - C_x C_y]^\top$$

where $\vartheta \in \mathbb{R}_+$ is a positive constant. Based on Γ_d , an enhanced-coupling signal is utilized to design the outer loop controller in the following manner as:

$$\mathbf{s} = \gamma - \Gamma_d = \gamma - (\gamma_d + \vartheta [S_x C_y, S_y, 1 - C_x C_y]^\top) \\ = e_\gamma - \vartheta [S_x C_y, S_y, 1 - C_x C_y]^\top$$

$$= e_\gamma - \boldsymbol{\mu} \quad (24)$$

where the payload swing angle information item $\boldsymbol{\mu}$ is defined as $\boldsymbol{\mu} = \vartheta[S_x C_y, S_y, 1 - C_x C_y]^\top$. Taking the time derivative of the composite signal (24) yields

$$\begin{aligned} \frac{d\boldsymbol{\zeta}}{dt} &= \frac{de_\gamma}{dt} - \frac{d\boldsymbol{\mu}}{dt} = \frac{de_\gamma}{dt} - \vartheta \left[\frac{d(S_x C_y)}{dt}, \frac{dS_y}{dt}, \frac{d(1 - C_x C_y)}{dt} \right]^\top \\ \Rightarrow \dot{\boldsymbol{\zeta}} &= \dot{e}_\gamma - \dot{\boldsymbol{\mu}} = \dot{e}_\gamma - \vartheta \begin{bmatrix} \dot{\theta}_x C_x C_y - \dot{\theta}_y S_x S_y \\ \dot{\theta}_y C_y \\ \dot{\theta}_x S_x C_y + \dot{\theta}_y C_x S_y \end{bmatrix} \end{aligned} \quad (25)$$

from which one can obtain that

$$\|\boldsymbol{\mu}\| \leq 2\vartheta, \|\dot{\boldsymbol{\mu}}\| \leq \vartheta \sqrt{\dot{\theta}_x^2 + \dot{\theta}_y^2}. \quad (26)$$

1) Outer Loop Controller Design: According to the outer loop dynamic model (1) and the result $\dot{e}_q = \dot{\boldsymbol{q}}$, $\ddot{e}_q = \ddot{\boldsymbol{q}}$, the open-loop error dynamics can be expressed as

$$\ddot{e}_q = M_c^{-1}(\boldsymbol{u} + \boldsymbol{F}_{q\text{dis}} - V_c \dot{e}_q - \boldsymbol{G}). \quad (27)$$

The energy of the outer loop system takes the following form:

$$E = \frac{1}{2} \dot{e}_q^\top M_c \dot{e}_q + mgl(1 - C_x C_y). \quad (28)$$

Subsequently, according to Property 1, taking the time derivative of (28), and inserting (27) yields

$$\begin{aligned} \dot{E} &= \dot{e}_q^\top \left(\frac{1}{2} \dot{M}_c \dot{e}_q + M_c \ddot{e}_q \right) + mgl \left(\dot{\theta}_x S_x C_y + \dot{\theta}_y C_x S_y \right) \\ &= \dot{e}_q^\top \left(\frac{1}{2} \dot{M}_c - V_c \right) \dot{e}_q + \dot{e}_q^\top (\boldsymbol{u} + \boldsymbol{F}_{q\text{dis}}) - \dot{e}_q^\top \boldsymbol{G} \\ &\quad + mgl \left(\dot{\theta}_x S_x C_y + \dot{\theta}_y C_x S_y \right) \\ &= \dot{e}_q^\top (\boldsymbol{u} + \boldsymbol{F}_{q\text{dis}}) - (M + m)g\dot{e}_z \\ &= [\dot{e}_q^\top, \dot{\boldsymbol{\Theta}}^\top] \left([f R e_3 - (M + m)g e_3, 0, 0]^\top + \boldsymbol{F}_{q\text{dis}} \right) \\ &= \dot{e}_q^\top [f R e_3 - (M + m)g e_3 + (M + m)\boldsymbol{a}_{\text{dis}}]. \end{aligned} \quad (29)$$

Utilizing the composite position signal (24), a nonnegative function E_n is constructed, whose time derivative is given as

$$\begin{aligned} \dot{E}_n &= \dot{\boldsymbol{\zeta}}^\top [f R e_3 - (M + m)g e_3 + (M + m)\boldsymbol{a}_{\text{dis}}] \\ &= \dot{E} + \dot{E}_\vartheta. \end{aligned} \quad (30)$$

Therewith, combining with (4)–(8), the expression of \dot{E}_ϑ can be further written as

$$\begin{aligned} \dot{E}_\vartheta &= -\dot{\boldsymbol{\mu}}^\top [f R e_3 - (M + m)g e_3 + (M + m)\boldsymbol{a}_{\text{dis}}] \\ &= -\vartheta(M + m)\dot{\theta}_x (\ddot{x} C_x C_y + \ddot{z} S_x C_y) - \vartheta(M + m)\dot{\theta}_y \\ &\quad \times (-\ddot{x} S_x S_y + \ddot{y} C_y + \ddot{z} C_x S_y) - \vartheta \left(\dot{\theta}_x C_x C_y - \dot{\theta}_y S_x S_y \right) \\ &\quad \times ml \left(\ddot{\theta}_x C_x C_y - \ddot{\theta}_y S_x S_y - \dot{\theta}_x^2 S_x C_y - \dot{\theta}_y^2 S_x C_y - 2\dot{\theta}_x \dot{\theta}_y C_x S_y \right) \\ &\quad - \vartheta \dot{\theta}_y C_y ml \left(\ddot{\theta}_y C_y - \dot{\theta}_y^2 S_y \right) - \vartheta \left(\dot{\theta}_x S_x C_y + \dot{\theta}_y C_x S_y \right) \\ &\quad \times ml \left(\ddot{\theta}_x S_x C_y + \ddot{\theta}_y C_x S_y + \dot{\theta}_x^2 C_x C_y + \dot{\theta}_y^2 C_x C_y - 2\dot{\theta}_x \dot{\theta}_y S_x S_y \right) \end{aligned}$$

$$\begin{aligned} &= \vartheta(M + m)l \left(\dot{\theta}_x \ddot{\theta}_x C_y^2 - \dot{\theta}_x^2 \dot{\theta}_y C_y S_y + \dot{\theta}_y \ddot{\theta}_y \right) + \vartheta(M + m) \\ &\quad \times g \left(\dot{\theta}_x S_x C_y + \dot{\theta}_y C_x S_y \right) - \vartheta ml \dot{\theta}_y C_y \frac{d}{dt} \left(\dot{\theta}_y C_y \right) \\ &\quad - \vartheta ml \left(\dot{\theta}_x C_x C_y - \dot{\theta}_y S_x S_y \right) \frac{d}{dt} \left(\dot{\theta}_x C_x C_y - \dot{\theta}_y S_x S_y \right) \\ &\quad - \vartheta ml \left(\dot{\theta}_x S_x C_y + \dot{\theta}_y C_x S_y \right) \frac{d}{dt} \left(\dot{\theta}_x S_x C_y + \dot{\theta}_y C_x S_y \right) \\ &= \frac{1}{2} \vartheta(M + m)l \frac{d}{dt} \left(\dot{\theta}_x^2 C_y^2 + \dot{\theta}_y^2 \right) + \vartheta(M + m)g \frac{d}{dt} (1 - C_x C_y) \\ &\quad - \frac{1}{2} \vartheta ml \frac{d}{dt} \left(\dot{\theta}_x C_x C_y - \dot{\theta}_y S_x S_y \right)^2 - \frac{1}{2} \vartheta ml \frac{d}{dt} \left(\dot{\theta}_y C_y \right)^2 \\ &\quad - \frac{1}{2} \vartheta ml \frac{d}{dt} \left(\dot{\theta}_x S_x C_y + \dot{\theta}_y C_x S_y \right)^2. \end{aligned} \quad (31)$$

Therefore, integrating (31) with respect to time, E_ϑ can be chosen as

$$E_\vartheta = \frac{1}{2} \vartheta M l \left(\dot{\theta}_x^2 C_y^2 + \dot{\theta}_y^2 \right) + \vartheta(M + m)g(1 - C_x C_y) \quad (32)$$

which is positive obviously. Furthermore, construct the following positive definite function:

$$V = E_n + \boldsymbol{k}_p^\top \text{Ln} [\text{Cosh}(\boldsymbol{\zeta})] \quad (33)$$

where $\boldsymbol{k}_p = [k_{px}, k_{py}, k_{pz}]^\top \in \mathbb{R}_+^3$ is a gain vector. Taking the time derivative of (33) yields

$$\begin{aligned} \dot{V} &= \dot{\boldsymbol{\zeta}}^\top [f R e_3 - (M + m)g e_3 + (M + m)\boldsymbol{a}_{\text{dis}} + K_p \text{Tanh}(\boldsymbol{\zeta})] \\ &= \dot{\boldsymbol{\zeta}}^\top [f_\gamma + f_\Delta - (M + m)g e_3 + (M + m)\boldsymbol{a}_{\text{dis}} \\ &\quad + K_p \text{Tanh}(\boldsymbol{\zeta})] \end{aligned} \quad (34)$$

wherein $K_p = \text{diag}(\boldsymbol{k}_p) \in \mathbb{R}_+^{3 \times 3}$, the constructed virtual control input f_γ and the auxiliary vector f_Δ are given as $f_\gamma = (f / (e_3^\top R_d^\top R e_3)) R_d e_3$, $f_\Delta = (f / (e_3^\top R_d^\top R e_3)) [(e_3^\top R_d^\top R e_3) R e_3 - R_d e_3]$. Based on the idea of hierarchical control, vector f_Δ reflects the coupling between the multirotor's translation and rotation, which can be temporarily neglected. Thus, from (34), the virtual control input f_γ is constructed as follows:

$$f_\gamma = -K_p \text{Tanh}(\boldsymbol{\zeta}) - K_d \text{Tanh}(\dot{\boldsymbol{\zeta}}) - (M + m)\hat{\boldsymbol{a}}_{\text{dis}} + (M + m)g e_3 \quad (35)$$

where $K_d = \text{diag}([k_{dx}, k_{dy}, k_{dz}]) \in \mathbb{R}_+^{3 \times 3}$ is a positive definite diagonal matrix.

Afterward, according to the relation $f_\gamma = (f / (e_3^\top R_d^\top R e_3)) R_d e_3$, it is obvious that f_γ and $R_d e_3$ have the same direction; thus, the desired unit direction vector $r_{3d} = R_d e_3 \in \mathbb{R}^3$ can be obtained by calculating $r_{3d} = R_d e_3 = f_\gamma / \|f_\gamma\|$. So f_γ can be further arranged as

$$f_\gamma = \frac{f \|f_\gamma\|}{f_\gamma^\top R e_3} \cdot \frac{f_\gamma}{\|f_\gamma\|} = \frac{f \cdot f_\gamma}{f_\gamma^\top R e_3} \Rightarrow f_\gamma^\top R e_3 \cdot f_\gamma = f \cdot f_\gamma$$

which indicates that the scaler multirotor thrust can be calculated by

$$f = f_\gamma^\top R e_3. \quad (36)$$

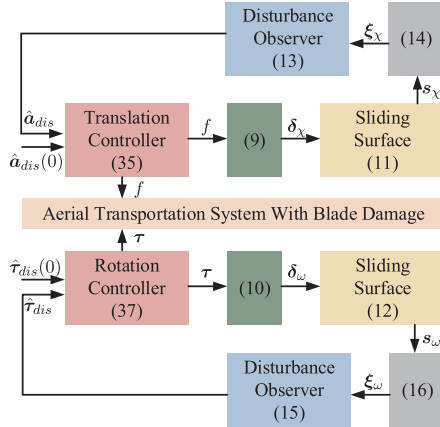


Fig. 3. Block diagram of the calculation process of the finite-time disturbance observer.

Thus, according to (35) and (36), the final scaler multirotor thrust is

$$f = (-K_p \text{Tanh}(\zeta) - K_d \text{Tanh}(\dot{\zeta}) - (M + m)\hat{a}_{\text{dis}} + (M + m)ge_3)^\top Re_3.$$

Then, on the basis of the obtained unit vector r_{3d} , selecting an arbitrary vector $r_{1a}(t) \in \mathbb{R}^3$ not parallel to r_{3d} , the desired attitude can be derived as $R_d(t) = [r_{2d} \times r_{3d}; r_{2d}; r_{3d}]$, where $r_{2d} = \frac{r_{3d} \times r_{1a}}{\|r_{3d} \times r_{1a}\|}$ represents the second row of the desired rotation matrix. Subsequently, the desired angular velocity can be presented as $\Omega_d = \text{vex}(R_d^\top \dot{R}_d)$ [10], [32], [36], [37].

2) Inner Loop Controller Design: For the inner loop of the system, the following nonlinear attitude controller is described by moment vector as follows:

$$\tau = -k_R e_R - k_\Omega e_\Omega - \hat{\tau}_{\text{dis}} + \text{sk}(\Omega)J\Omega - J(\text{sk}(\Omega)R^\top R_d \Omega_d - R^\top R_d \dot{\Omega}_d) \quad (37)$$

wherein $k_R, k_\Omega \in \mathbb{R}$ are positive constants.

Similar to other disturbance observers in [38], the main calculation process of the finite-time disturbance observer is provided in Fig. 3.

Remark 4: Due to the underactuated characteristic caused by the payload swing motion, the direct derivation of the backstepping controller will be much complicated. In this article, based on the theory on cascade systems, the controller designs are carried out for the inner loop and outer loop subsystems, respectively. Compared to the control scheme based on backstepping technique [39], [40], the proposed method has a concise form and greatly simplifies the design difficulty.

C. Stability Analysis

In this section, by neglecting the coupling term f_Δ , the stability of the inner loop and outer loop subsystems are first proved, respectively. Then, based on the theory of cascade systems, the stability of the closed-loop system is obtained by proving the

coupling term satisfies the growth restriction condition [10], [41], [42].

Theorem 2: Under the designed attitude controller (37) and the disturbance observer (15) and (16), the attitude error dynamics is bounded and converges to zero, i.e.,

$$\lim_{t \rightarrow \infty} e_R = \mathbf{0}_{3 \times 1}, \quad \lim_{t \rightarrow \infty} e_\Omega = \mathbf{0}_{3 \times 1}.$$

Proof: To prove Theorem 2, select the following Lyapunov function candidate for the rotational motion as:

$$V_r = \frac{1}{2} e_\Omega^\top J e_\Omega + k_R \Xi(R, R_d) + \varrho e_R^\top e_\Omega + \frac{1}{2} (J^{-1} \tilde{\tau}_{\text{dis}})^\top (J^{-1} \tilde{\tau}_{\text{dis}}) \quad (38)$$

where $\Xi(R, R_d) = \frac{1}{2} \text{tr}[I - R_d^\top R]$ is the real-valued error function defined on $SO(3) \times SO(3)$, and ϱ is a positive constant that satisfies $\varrho < \min\{k_\Omega, \frac{4k_\Omega k_R \lambda_m(J)^2}{k_\Omega^2 \lambda_M(J) + 4k_R \lambda_m(J)^2}, \sqrt{k_R \lambda_m(J)}\}$. The Lyapunov function candidate (38) is proved to be positive definite [32], [36]. Taking the time derivative of the attitude and angular velocity tracking errors, one has

$$\begin{aligned} \dot{e}_R &= C(R_d^\top R) e_\Omega \\ J \dot{e}_\Omega &= \tau + \tau_{\text{dis}} - \text{sk}(\Omega)J\Omega \\ &\quad + J(\text{sk}(\Omega)R^\top R_d \Omega_d - R^\top R_d \dot{\Omega}_d) \end{aligned} \quad (40)$$

where $C(R_d^\top R) = \frac{1}{2}(\text{tr}[R^\top R_d]I - R^\top R_d)$ and satisfies $\|C(R_d^\top R)\| < 1$, for $\forall R_d^\top R \in SO(3)$.

By substituting (39), (40), and (37) into the time derivative of (38), and considering (15) and $s_\omega = J^{-1} \tau_{\text{dis}} - \xi_\omega$, one obtains

$$\begin{aligned} \dot{V}_r &= e_\Omega^\top J \dot{e}_\Omega + k_R e_R^\top e_\Omega + \varrho \dot{e}_R^\top e_\Omega + \varrho e_R^\top \dot{e}_\Omega \\ &\quad + (J^{-1} \tilde{\tau}_{\text{dis}})^\top (J^{-1} \dot{\tilde{\tau}}_{\text{dis}}) \\ &= -k_\Omega e_\Omega^\top e_\Omega + \varrho C(R_d^\top R) e_\Omega^\top e_\Omega - \varrho k_R J^{-1} e_R^\top e_R \\ &\quad - \varrho k_\Omega J^{-1} e_R^\top e_\Omega + (e_\Omega^\top + \varrho J^{-1} e_R^\top) \tilde{\tau}_{\text{dis}} + s_\omega^\top \dot{s}_\omega \\ &\leq -(k_\Omega - \varrho) \|e_\Omega\|^2 - \frac{\varrho k_R}{\lambda_M(J)} \|e_R\|^2 + \frac{\varrho k_\Omega}{\lambda_m(J)} \|e_R\| \|e_\Omega\| \\ &\quad + \|e_\Omega\| \|\tilde{\tau}_{\text{dis}}\| + \frac{\varrho}{\lambda_m(J)} \|e_R\| \|\tilde{\tau}_{\text{dis}}\| \\ &\quad - [\eta_{d\omega 1}, \eta_{d\omega 2}, \eta_{d\omega 3}] \|s_\omega\| \\ &\leq -(k_\Omega - \varrho) \|e_\Omega\|^2 - \frac{\varrho k_R}{\lambda_M(J)} \|e_R\|^2 + \frac{\varrho k_\Omega}{\lambda_m(J)} \|e_R\| \|e_\Omega\| \\ &\quad + \|e_\Omega\| \|\tilde{\tau}_{\text{dis}}\| + \frac{\varrho}{\lambda_m(J)} \|e_R\| \|\tilde{\tau}_{\text{dis}}\|. \end{aligned} \quad (41)$$

Further, define the generalized attitude error vector $e_I = [\|e_R\|, \|e_\Omega\|]^\top$, (41) can be rewritten as

$$\begin{aligned} \dot{V}_r &\leq -e_I^\top W_1 e_I + \|\tilde{\tau}_{\text{dis}}\| W_2^\top e_I \\ &\leq -\lambda_m(W_1) \|e_I\|^2 + \|\tilde{\tau}_{\text{dis}}\| \|W_2\| \|e_I\| \end{aligned} \quad (42)$$

where in W_1 and W_2 take the following form as:

$$W_1 = \begin{bmatrix} \frac{\varrho k_R}{\lambda_M(J)} & -\frac{\varrho k_\Omega}{2\lambda_m(J)} \\ -\frac{\varrho k_\Omega}{2\lambda_m(J)} & k_\Omega - \varrho \end{bmatrix}, \quad W_2 = \left[\frac{\varrho}{\lambda_m(J)}, 1 \right]^\top.$$

Step 1: $t < t_{f\Omega}$. From (42), on one hand, when $\|e_I\| \geq \frac{\|W_2\|}{\lambda_m(W_1)} \|\tilde{\tau}_{\text{dis}}\|$, it is obvious that $\dot{V}_r \leq 0$, which means the attitude error is decreasing progressively. On the other hand, $\|e_I\| < \frac{\|W_2\|}{\lambda_m(W_1)} \|\tilde{\tau}_{\text{dis}}\|$ implies that the attitude error is bounded since $\tilde{\tau}_{\text{dis}}$ is bounded. Therefore, when $t < t_{f\Omega}$, the rotation error is bounded.

Step 2: $t \geq t_{f\Omega}$. When $t \geq t_{f\Omega}$, the disturbance estimate error is zero, i.e., $\tau_{\text{dis}} = \mathbf{0}_{3 \times 1}$. Thus, (42) turns to

$$\dot{V}_r \leq -\lambda_m(W_1) \|e_I\|^2$$

which indicates the attitude error dynamics will be exponentially stable [32], [36].

Collecting up the above two steps' analysis, one can conclude that Theorem 2 holds.

Theorem 3: The designed controller (35) and the disturbance observers (13) and (14) guarantee that the tracking error of the outer loop subsystem is bounded and converges to zero, i.e.,

$$\lim_{t \rightarrow \infty} \left[e_\gamma^\top, \Theta^\top, \dot{e}_\gamma^\top, \dot{\Theta}^\top \right]^\top = \left[\mathbf{0}_{3 \times 1}^\top, \mathbf{0}_{2 \times 1}^\top, \mathbf{0}_{3 \times 1}^\top, \mathbf{0}_{2 \times 1}^\top \right]^\top.$$

Proof: To prove Theorem 3, the Lyapunov function candidate is chosen as

$$V_t = V + \frac{1}{2} \tilde{\mathbf{a}}_{\text{dis}}^\top \tilde{\mathbf{a}}_{\text{dis}}. \quad (43)$$

Then, substituting (35) into the time derivative of (43), and noting (13) and $\mathbf{s}_\chi = \mathbf{a}_{\text{dis}} - \xi_\chi$ yields

$$\begin{aligned} \dot{V}_t &= \dot{\zeta}^\top [(M+m)\tilde{\mathbf{a}}_{\text{dis}} - K_d \text{Tanh}(\dot{\zeta})] + \tilde{\mathbf{a}}_{\text{dis}}^\top \dot{\tilde{\mathbf{a}}}_{\text{dis}} \\ &= -\dot{\zeta}^\top K_d \text{Tanh}(\dot{\zeta}) + \dot{\zeta}^\top (M+m)\tilde{\mathbf{a}}_{\text{dis}} + \tilde{\mathbf{s}}_\chi^\top \dot{\tilde{\mathbf{s}}}_\chi \\ &\leq -\dot{\zeta}^\top K_d \text{Tanh}(\dot{\zeta}) + \dot{\zeta}^\top (M+m)\tilde{\mathbf{a}}_{\text{dis}} - [\eta_{dx}, \eta_{dy}, \eta_{dz}] |s_\chi| \\ &\leq -\dot{\zeta}^\top K_d \text{Tanh}(\dot{\zeta}) + \dot{\zeta}^\top (M+m)\tilde{\mathbf{a}}_{\text{dis}}. \end{aligned} \quad (44)$$

Subsequently, the analysis is divided into two steps as follows.

Step 1: $t < t_{f\chi}$. From (44), one can derive that

$$\begin{aligned} \dot{V}_t &\leq -\|K_d\| \|\dot{\zeta}\|^2 + (M+m) \|\dot{\zeta}\| \|\tilde{\mathbf{a}}_{\text{dis}}\| \\ &= -\|\dot{\zeta}\| (\|K_d\| \|\dot{\zeta}\| - (M+m) \|\tilde{\mathbf{a}}_{\text{dis}}\|). \end{aligned}$$

Based on the above inequality, two cases will be analyzed, i.e., i) $\|\dot{\zeta}\| \geq \frac{M+m}{\|K_d\|} \|\tilde{\mathbf{a}}_{\text{dis}}\|$ and ii) $\|\dot{\zeta}\| < \frac{M+m}{\|K_d\|} \|\tilde{\mathbf{a}}_{\text{dis}}\|$.

- 1) For the first case $\|\dot{\zeta}\| \geq \frac{M+m}{\|K_d\|} \|\tilde{\mathbf{a}}_{\text{dis}}\|$, it is obvious that $\|K_d\| \|\dot{\zeta}\| - (M+m) \|\tilde{\mathbf{a}}_{\text{dis}}\| \geq 0$, which indicates that $\dot{V}_t \leq 0$. In this case, the outer loop error dynamics is decreasing progressively.
- 2) On the flip side, the second case $\|\dot{\zeta}\| < \frac{M+m}{\|K_d\|} \|\tilde{\mathbf{a}}_{\text{dis}}\|$ implies that the translation error is bounded since $\tilde{\mathbf{a}}_{\text{dis}}$ is bounded.

In summary, when $t < t_{f\chi}$, the translation error dynamics of the system is bounded.

Step 2: $t \geq t_{f\chi}$. Based on (23), (44) can be further deduced as

$$\dot{V}_t = -\dot{\zeta}^\top K_d \text{Tanh}(\dot{\zeta}) \leq 0. \quad (45)$$

Integrating (45) with respect to time, one has

$$V_t(t) = V_t(t_{f\chi}) - \int_{t_{f\chi}}^t \dot{\zeta}^\top K_d \text{Tanh}(\dot{\zeta}) d\tau \leq V_t(t_{f\chi}) \ll +\infty \quad (46)$$

then combining with (28), (32), and (33) yields

$$V_t(t) \in \mathcal{L}_\infty \Rightarrow \zeta, \dot{\zeta}, \dot{\theta}_x, \dot{\theta}_y \in \mathcal{L}_\infty. \quad (47)$$

Thus, with the result in (47) and (26), from (24), (35), and the system models (4)–(8), one achieves $\gamma, \dot{\gamma}, \dot{\zeta} \in \mathcal{L}_\infty$. Define a set $\Psi = \{(e_\gamma, \dot{e}_\gamma, \theta_x, \theta_y, \dot{\theta}_x, \dot{\theta}_y) \mid \dot{V}_t(t) = 0\}$, let Λ be the largest invariant set in Ψ . Subsequently, combining with (45), one can conclude that

$$\dot{\zeta} = \mathbf{0}_{3 \times 1}. \quad (48)$$

From (48), it is derived

$$\zeta = \varpi_1, \ddot{\zeta} = \mathbf{0}_{3 \times 1} \quad (49)$$

where $\varpi_1 = [\varpi_{1x}, \varpi_{1y}, \varpi_{1z}]^\top$ represents an undetermined constant vector. Then, substituting (35), (48), and (49) into system models (4)–(6) and making some transformation yields

$$\dot{\gamma} = -\frac{[\vartheta k_{px} \tanh(\varpi_{1x}), \vartheta k_{py} \tanh(\varpi_{1y}), \vartheta k_{pz} \tanh(\varpi_{1z})]}{\vartheta(M+m) + ml}.$$

Assuming $\varpi_{1x} \neq 0, \varpi_{1y} \neq 0, \varpi_{1z} \neq 0$, one can conclude that $\dot{x} \rightarrow \infty, \dot{y} \rightarrow \infty, \dot{z} \rightarrow \infty$ as $t \rightarrow \infty$, which conflicts with the conclusion $\dot{\gamma} \in \mathcal{L}_\infty$. Therefore, the assumption $\varpi_{1x} \neq 0, \varpi_{1y} \neq 0, \varpi_{1z} \neq 0$ does not hold, and one can deduce that

$$\varpi_1 = \mathbf{0}_{3 \times 1} \Rightarrow \zeta = \mathbf{0}_{3 \times 1}, \mathbf{f}_\gamma = (M+m)g\mathbf{e}_3 \quad (50)$$

$$\dot{\gamma} = \mathbf{0}_{3 \times 1} \Rightarrow \dot{e}_\gamma = \varpi_2 \quad (51)$$

where $\varpi_2 = [\varpi_{2x}, \varpi_{2y}, \varpi_{2z}]^\top$ represents an undetermined constant vector. In an analogous method, assuming $\varpi_{2x} \neq 0, \varpi_{2y} \neq 0, \varpi_{2z} \neq 0$, it can be derived that $x \rightarrow \infty, y \rightarrow \infty, z \rightarrow \infty$ as $t \rightarrow \infty$, which is inconsistent with $\gamma \in \mathcal{L}_\infty$. Thus, one has

$$\varpi_2 = \mathbf{0}_{3 \times 1} \Rightarrow \dot{e}_\gamma = \mathbf{0}_{3 \times 1}. \quad (52)$$

Subsequently, with the result in (48) and (52), it is found that

$$\dot{\theta}_x C_x C_y - \dot{\theta}_y S_x S_y = 0, \dot{\theta}_y C_y = 0, \dot{\theta}_x S_x C_y + \dot{\theta}_y C_x S_y = 0. \quad (53)$$

According to Assumption 1 and (53), it is obvious that

$$\dot{\theta}_x = 0, \dot{\theta}_y = 0 \Rightarrow \ddot{\theta}_x = 0, \ddot{\theta}_y = 0. \quad (54)$$

Substituting (52) and (54) into (7) and (8) achieves

$$mglS_x C_y = 0, mglC_x S_y = 0 \Rightarrow \theta_x = 0, \theta_y = 0. \quad (55)$$

Finally, substituting (55) into the result $\zeta = \mathbf{0}_{3 \times 1}$ yields

$$e_\gamma = \mathbf{0}_{3 \times 1}. \quad (56)$$

In summary, (52), (54), (55), and (56) show that Theorem 3 holds. ■

After the stability analysis of the inner loop and outer loop subsystems without considering the coupling term as presented

in Theorems 2 and 3, the characteristics of the coupling term will be further analyzed in Theorem 4.

Theorem 4: The proposed control law (35) and (37) and the disturbance observers (13)–(16) can drive the multirotor to the desired position, while suppressing the payload swing even with blade damage, implying the following result:

$$\lim_{t \rightarrow \infty} \begin{bmatrix} e_\gamma^\top, \dot{e}_\gamma^\top, \Theta^\top, \dot{\Theta}^\top, e_R^\top, e_\Omega^\top \end{bmatrix}^\top \\ = \begin{bmatrix} \mathbf{0}_{3 \times 1}^\top, \mathbf{0}_{3 \times 1}^\top, \mathbf{0}_{2 \times 1}^\top, \mathbf{0}_{2 \times 1}^\top, \mathbf{0}_{3 \times 1}^\top, \mathbf{0}_{3 \times 1}^\top \end{bmatrix}^\top.$$

Proof: The stability analysis of the overall closed-loop system with the consideration of the coupling term f_Δ is taken into account here. Define the generalized translation error vector as $e_O = [e_q^\top, \dot{e}_q^\top]^\top$. Inserting $R_d e_3 = \frac{f_\gamma}{\|f_\gamma\|}$ and $f = f_\gamma^\top R e_3$ into f_Δ , and according to [32], one can conclude that

$$\|f_\Delta\| = \|f_\gamma\| \left\| (e_3^\top R_d^\top R e_3) R e_3 - R_d e_3 \right\| \\ \leq \|f_\gamma\| \|e_R\|. \quad (57)$$

Since the lumped disturbance is caused by blade damage, and the disturbance observers (13) and (14) can estimate the disturbance unbiasedly in finite-time, thus according to Assumption 3, define the upper bound as $\|\hat{a}_{\text{dis}}\| \leq a$, where a is a positive constant. Based on the result in (26), and the fact that $|\tanh(\cdot)| < |\cdot|$, the virtual control input (35) satisfies that

$$\|f_\gamma\| \leq \|K_p \varsigma\| + \|K_d \dot{\varsigma}\| + (M + m)g + (M + m)a \\ \leq 2 \max(\lambda_M(K_p), \lambda_M(K_d)) \cdot \max(1, \vartheta) \|e_O\| \\ + (M + m)g + (M + m)a + 2k_\lambda \max(\lambda_M(K_p), \lambda_M(K_d)) \\ = \left(\|e_O\| + \frac{(M + m)(g + a) + 2k_\lambda \max(\lambda_M(K_p), \lambda_M(K_d))}{2 \max(\lambda_M(K_p), \lambda_M(K_d)) \cdot \max(1, \vartheta)} \right) \\ \cdot 2 \max(\lambda_M(K_p), \lambda_M(K_d)) \cdot \max(1, \vartheta).$$

By setting $\varepsilon = 4 \max(\lambda_M(K_p), \lambda_M(K_d)) \cdot \max(1, \vartheta)$, $\varepsilon = \frac{(M + m)(g + a) + 2k_\lambda \max(\lambda_M(K_p), \lambda_M(K_d))}{2 \max(\lambda_M(K_p), \lambda_M(K_d)) \cdot \max(1, \vartheta)}$, one knows that the virtual control vector f_γ satisfies the following property:

$$\|f_\gamma(e_O)\| \leq \begin{cases} \varepsilon \|e_O\|, & \text{for } \|e_O\| \geq \varepsilon \\ \varepsilon, & \text{for } \|e_O\| < \varepsilon \end{cases}. \quad (58)$$

Then, substituting the result of (58) into (57), the coupling term can be further deduced as

$$\|f_\Delta\| \leq \|f_\gamma\| \|e_R\| \\ \leq \varepsilon \|e_O\| \|e_R\|, \text{ for } \|e_O\| \geq \varepsilon$$

which means that the coupling term f_Δ satisfies the growth restriction condition. Thus, as shown in [10], [41], [42], the stability of the overall system can be proven. ■

Remark 5: It is worth noting that the proposed control scheme can not only achieve multirotor positioning but also realize constant velocity trajectory tracking. When tracking a constant velocity trajectory, the time derivatives of the desired trajectory are $\dot{q}_d = [c_x, c_y, c_z, 0, 0]$, $\ddot{q}_d = \mathbf{0}_{5 \times 1}$, where c_x, c_y, c_z are constants. Thus, $M_c \ddot{q}_d = 0$. According to the form of the centripetal–Coriolis matrix V_c , one can calculate that $V_c \dot{q}_d = 0$.

Therefore, the open-loop error dynamics of the outer loop subsystem can be arranged as

$$M_c \ddot{e}_q + M_c \ddot{q}_d + V_c \dot{e}_q + V_c \dot{q}_d + G = u + F_{q_{\text{dis}}} \\ \Rightarrow \ddot{e}_q = M_c^{-1} (u + F_{q_{\text{dis}}} - V_c \dot{e}_q - G).$$

Then, the subsequent controller design and analysis process is similar to the process of regulation problem.

IV. SIMULATION AND EXPERIMENTAL IMPLEMENTATION

In this section, simulation and experimental tests are implemented to verify the feasibility of the proposed tracking controller.

A. Numerical Simulation and Analysis

Numerical simulation tests are first carried out in MATLAB/Simulink to verify the designed control law's performance.

1) Blade Damage During Hovering: The physical parameters of the aerial transportation system are set as $M = 0.625$ kg, $m = 0.075$ kg, $l = 0.5$ m, $g = 9.8$ m/s², $J = \text{diag}([0.01379, 0.01379, 0.02507])$ kg · m², $d = 0.225$ m, $c_T = 1.201 \times 10^{-5}$ N/(rad/s)², $c_\tau = 1.606 \times 10^{-7}$ N · m/(rad/s)². The control gains of the designed control scheme are selected as $K_p = \text{diag}([1.0, 1.0, 1.2])$, $K_d = \text{diag}([2.5, 2.5, 2.8])$, $\vartheta = 1.5$, $k_R = 5.0$, $k_\Omega = 0.6$, $c_{\alpha_\chi} = \text{diag}([5.0, 5.0, 5.0])$, $c_{\beta_\chi} = \text{diag}([5.0, 5.0, 5.0])$, $c_{\alpha_\omega} = \text{diag}([2.0, 2.0, 2.0])$, $c_{\beta_\omega} = \text{diag}([1.0, 1.0, 1.0])$, $\alpha_\chi = 0.5$, $\beta_\chi = 2$, $\alpha_\omega = 0.5$, $\beta_\omega = 2$, $\eta_{d_\chi} + \kappa_{d_\chi} = \text{diag}([0.5, 0.5, 15])$, $\eta_{d_\omega} + \kappa_{d_\omega} = \text{diag}([40.0, 40.0, 5.0])$. The initial and the desired position of the quadrotor are set as $\gamma_0 = [-0.5, 1.3, 1.0]^\top$ m and $\gamma_d = [0.5, 0.3, 1.5]^\top$ m. For the sake of description, define $[\hat{d}_x, \hat{d}_y, \hat{d}_z]^\top = (M + m)\hat{a}_{\text{dis}}$, $[\hat{d}_{\Omega_1}, \hat{d}_{\Omega_2}, \hat{d}_{\Omega_3}]^\top = \hat{\tau}_{\text{dis}}$. The blades of the first and the second propeller are damaged at 10 and 20s. The first one is broken by 30%, and the second one is broken by 20%. According to Remark 2, the lift and torque coefficients of the first propeller will suddenly decrease by 65.7% and 75.99%, and the lift and torque coefficients of the second propeller will suddenly decrease by 48.8% and 59.04%, respectively. Two control schemes are chosen for comparison to demonstrate the proposed method's payload swing elimination capability and disturbance rejection ability, respectively. One is the saturated PD controller f_{c1} combined with the designed finite-time disturbance observer

$$f_{c1} = -K_p \text{Tanh}(e_\gamma) - K_d \text{Tanh}(\dot{e}_\gamma) \\ + (M + m)g e_3 - (M + m)\hat{a}_{\text{dis}}$$

the other is the enhanced coupling method f_{c2} without the designed finite-time disturbance observer

$$f_{c2} = -K_p \text{Tanh}(\varsigma) - K_d \text{Tanh}(\dot{\varsigma}) + (M + m)g e_3.$$

The control gains of the two control schemes are selected the same as the proposed method. The simulation results are illustrated in Fig. 4, from which one can find that when the blades are suddenly damaged, the payload of the saturated PD controller with the designed finite-time disturbance observer produces large oscillations, and the quadrotor of the enhanced coupling

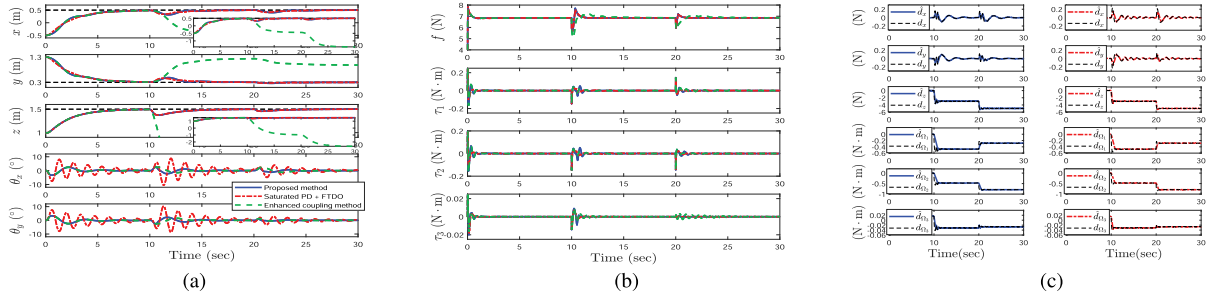


Fig. 4. Results for blade damage during hovering. (a) Quadrotor position and payload swing angles. (b) Control inputs. (c) Estimated disturbance forces and torques.

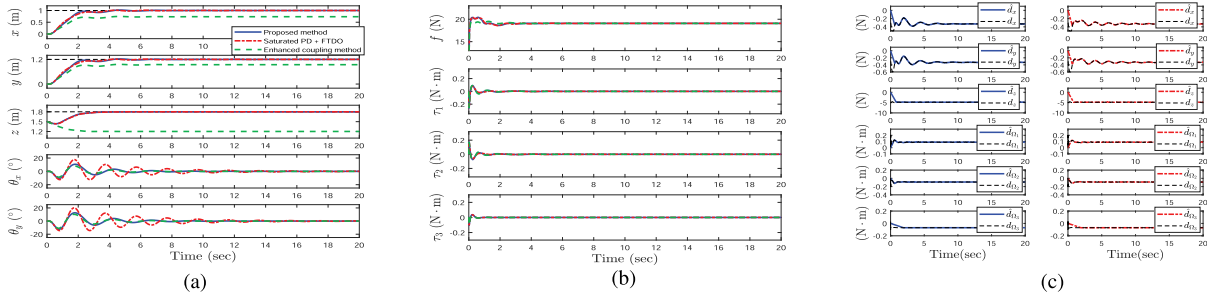


Fig. 5. Results for flight under blade damage. (a) Quadrotor position and payload swing angles. (b) Control inputs. (c) Estimated disturbance forces and torques.

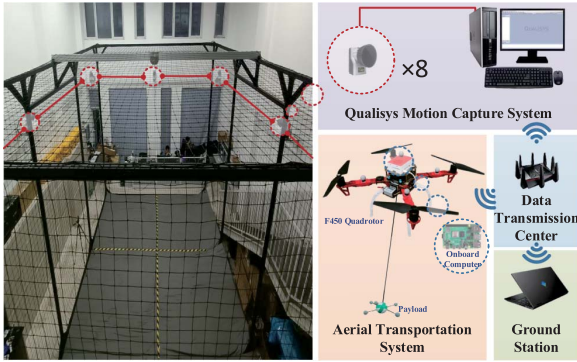


Fig. 6. Experimental platform.

method has significant positioning errors. On the contrary, the proposed method has shown good results in both quadrotor positioning and payload swing suppression, which indicates the designed controller can effectively overcome blade damage and ensure system safety. Specifically, as shown in Fig. 4(c), the designed finite-time observer can quickly estimate the lumped disturbances to their actual values.

2) Flight Under Blade Damage: To further verify the performance of the proposed method, this part refers to the hardware platform and selects the physical parameters as $M = 1.46$ kg, $m = 0.18$ kg, $l = 0.98$ m, $g = 9.8$ m/s², $J = \text{diag}([0.0117, 0.0120, 0.0184])$ kg · m². The parameters of the control algorithm are selected as $\vartheta = 0.2$, $K_p = \text{diag}([5.0, 5.0,$

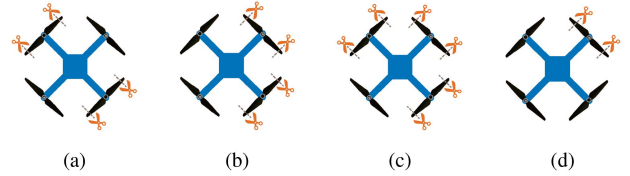


Fig. 7. To comprehensively verify the performance of the proposed method, four different types of blade damage are imitated. (a) Two opposite blades damage. (b) Two adjacent blades damage. (c) Three blades damage. (d) One blade damage.

8.0]), $K_d = \text{diag}([6.0, 6.0, 8.0])$, $k_R = 1.92$, $k_\Omega = 0.3$, $c_{\alpha_x} = \text{diag}([5.0, 5.0, 5.0])$, $c_{\beta_x} = \text{diag}([5.0, 5.0, 5.0])$, $c_{\alpha_\omega} = \text{diag}([2.0, 2.0, 2.0])$, $c_{\beta_\omega} = \text{diag}([1.0, 1.0, 1.0])$, $\alpha_x = 0.5$, $\beta_x = 2$, $\alpha_\omega = 0.5$, $\beta_\omega = 2$, $\eta_{d_x} + \kappa_{d_x} = \text{diag}([0.35, 0.35, 3.50])$, $\eta_{d_\omega} + \kappa_{d_\omega} = \text{diag}([20.0, 20.0, 2.0])$. The initial and the desired position of the quadrotor are set as $\gamma_0 = [0.0, 0.0, 1.5]^\top$ m and $\gamma_d = [1.0, 1.2, 1.8]^\top$ m. The blades of the second propeller are damaged at the beginning, resulting in a 10% breakage, which leads to a decrease of 27.1% in lift coefficient and 34.39% in torque coefficient. The saturated PD controller f_{c1} combined with the designed finite-time disturbance observer and the enhanced coupling method f_{c2} are selected as the comparison methods, whose control gains are chosen the same as the proposed method. The simulation results are presented in Fig. 5, from which one can find that under the blades damage, the comprehensive performance of the proposed method for quadrotor positioning and payload antiswing is superior to the other two methods.

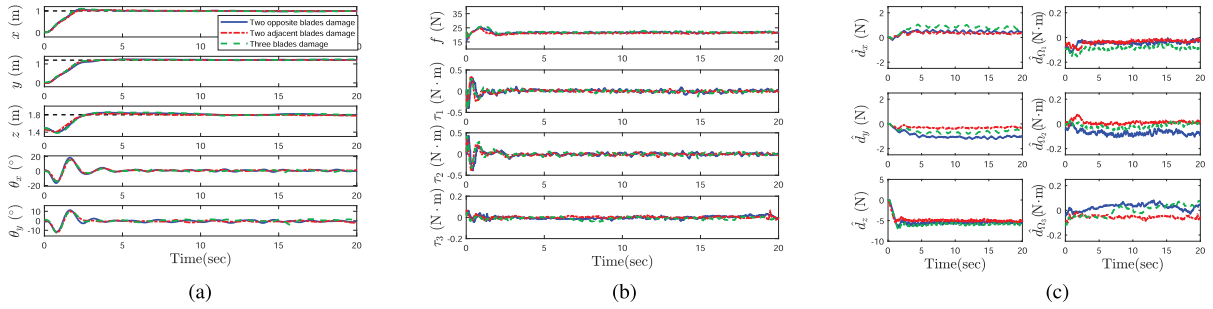


Fig. 8. Results for basic performance test. (a) Quadrotor position and payload swing angles. (b) Control inputs. (c) Estimated disturbance forces and torques.

B. Experimental Implementation

To further validate the performance and superiority of the proposed control scheme, in this section, two groups of experiments are carried out on the self-built hardware experiment platform.

1) Experimental Platform: As shown in Fig. 6, the experimental platform contains the aerial transportation system, the Qualisys motion capture system, the ground station and the data transmission center. The aerial transportation system is built through a multirotor and a cable-suspended 3-D-printed payload. Specifically, an F450 quadrotor is selected as the multirotor to complete the experiment, which is equipped with a PixHawk flight controller connecting to the onboard computer through MAVROS-based communication protocol. Qualisys motion capture system with eight cameras is employed to measure the quadrotor's translation motion, the yaw angle, and the payload swing angles by identifying the markers on the quadrotor and the payload. The ground station runs the 64-bit Ubuntu 18.04 operating system, which is utilized to send the desired position of the quadrotor with the support of the Robot Operating System. The data transmission center is supported by a router, which is responsible for exchanging all data in the experiment process.

It should be noted that in order to reduce the severe chattering caused by the sign function appearing in the disturbance observer, we replace $\text{sgn}(\iota)$ with $\tanh(k \times \iota)$ during the experimental implementation, where k is chosen as 10. The physical parameters and control gains are same as in Section IV-A2. The control frequency of the experiment is 100 Hz. In the following two sections, a basic performance test as well as a comparison test is implemented on the experimental platform. To verify the performance of the proposed method under different conditions and lengths of blade damage, several kinds of blade damage cases are imitated as illustrated in Fig. 7. As these cases can bring different disturbance effects, the performance of the control scheme will be more comprehensive. The experimental video is available in <https://youtu.be/6yWFeBSmOqs>.

2) Basic Performance Test: This part presents the basic performance verification for the designed control scheme. The control objective is to drive the quadrotor to the desired position while suppressing the payload swing simultaneously with damaged blades. The initial and the desired position of the quadrotor are set as $\gamma_0 = [0.0, 0.0, 1.5]^T$ m and $\gamma_d = [1.0, 1.2, 1.8]^T$ m. Three different conditions are tested as shown in Fig. 7(a)–(c),

including the damage of two opposite blades, two adjacent blades, and three blades. The damaged blade is obtained by cutting 1cm from each side of the normal propeller in this experiment. The experiment curves are presented in Fig. 8, from which one can figure out that even under different levels of blade damage, the designed control law can drive the quadrotor to the desired position while suppressing the payload swing fleetly. Therefore, from the experimental results, one can conclude that the designed fault-tolerant control scheme can compensate for the loss of the quadrotor force and torque, and deal with different situations of blades damage effectively.

3) Comparison Test: To further illustrate the performance of the proposed method, a comparative experiment is given in this part. The saturated PD controller f_{c1} combined with the designed finite-time disturbance observer and the enhanced coupling method f_{c2} without the designed finite-time disturbance observer are selected as comparison in the experiment, and the control gains of the two controllers are selected the same as the proposed method. The initial and the desired positions of the quadrotor are set the same as the basic performance test. In this test, only one propeller is damaged as shown in Fig. 7(d), which is obtained by cutting 2 cm from each side of the normal blade. Fig. 9 provides the curves of the proposed controller and the comparative ones. It should be noted that when the aerial transportation system hovers, the gravity of the system is equal to the lift force generated by the multirotor. Thus, the final control input signals of the three methods are almost the same. Besides, the explicit quantified data are recorded in Table II. From the rise time, one knows that the response speed of the three methods is almost the same. Under the similar response speed, the proposed method and the enhanced coupling method can effectively suppress the payload swing, while the saturated PD method combined with the designed finite-time disturbance observer has large payload oscillations. However, although the enhanced coupling method can suppress the payload swing, it cannot drive the quadrotor to the desired position, especially for the altitude, whose steady-state error reaches 0.4956 m, which further verifies that the designed disturbance observer can cope with blade damage efficaciously. In summary, at the similar response speed, compared with the other two methods, the proposed controller can deal with blade damage and realize payload swing suppression and quadrotor positioning simultaneously.

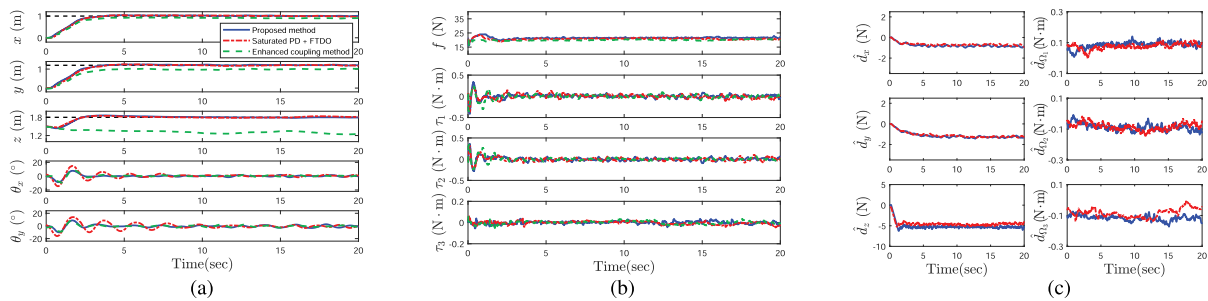


Fig. 9. Results for comparison test. (a) Quadrotor position and payload swing angles. (b) Control inputs. (c) Estimated disturbance forces and torques.

TABLE II
QUANTITATIVE DATA OF COMPARISON TEST

Comparison Test	Steady-state error (m)			Rise time (s)			Maximum value ($^{\circ}$)	
	e_x	e_y	e_z	t_x	t_y	t_z	θ_x	θ_y
Proposed method	0.0175	0.0184	0.0109	3.7	3.7	2.3	8.7739	10.0986
Saturated PD + FTDO	0.0191	0.0174	0.0134	3.7	3.9	2.4	14.8995	16.0612
Enhanced coupling method	0.0874	0.2078	0.4956	3.9	4.2	2.3	9.5731	9.1735

Remark 6: Considering the following two aspects: 1) the safety concerns and 2) comparison experiments require the same degree of blade damage. Therefore, it is hard to imitate blade damage in the actual flight process, so the damaged blades are directly utilized for experimental implementation similar to [28], [29], [43], [44], [45], and [46]. Due to the sudden blade damage, the upper bound of the time derivative of disturbance is high, so the range of D_k that we can select is relatively wide. Besides, the Lyapunov-based control design and analysis are conservative by nature, thus, the proposed control method may also work well in practice even if Assumption 4 is not rigorously satisfied.

Remark 7: In practice, the actual experimental platform cannot respond to the rapid changes in control inputs caused by sign functions, which leads to chattering phenomenon. As widely done in many literatures [31], [47], [48], [49], [50], [51], [52], [53], [54], [55], [56], [57], [58], [59], [60], the sign function is replaced by the hyperbolic tangent function in the experiment, which can greatly reduce input chattering.

V. CONCLUSION

To deal with the inevitable problem of blade damage in practical application, this article proposed a fault-tolerant control scheme for the cable-suspended aerial transportation systems. Particularly, by rewriting the form of the outer loop system model, a finite-time disturbance observer could be deliberately designed to estimate the disturbance caused by blade damage. Subsequently, an enhanced-coupling signal containing both payload swing angle and multirotor position was utilized to construct the outer loop control law, which greatly improved the payload antiswing performance. Under the framework of the cascade systems, Lyapunov techniques and LaSalle's invariance theorem were utilized to guarantee the stability of the closed-loop system. Experimental results demonstrated the remarkable performance of the proposed control scheme in swing suppression and multirotor positioning. In the ensuing research, we will

concentrate on designing more advanced control schemes to take care of uncertainties and measurement errors with theoretically robustness analysis and tend to develop fault-tolerant control methods for aerial transportation systems at the motor level capable of handling complete motor failure. Besides, we will further attempt to improve our observer to achieve stable control when the real-time signal feedback frequency is low.

REFERENCES

- [1] H. Wang, H. Ni, J. Wang, and W. Chen, "Hybrid vision/force control of soft robot based on a deformation model," *IEEE Trans. Control Syst. Technol.*, vol. 29, no. 2, pp. 661–671, Mar. 2021.
- [2] C. Yang, Y. Jiang, W. He, J. Na, Z. Li, and B. Xu, "Adaptive parameter estimation and control design for robot manipulators with finite-time convergence," *IEEE Trans. Ind. Electron.*, vol. 65, no. 10, pp. 8112–8123, Oct. 2018.
- [3] S. Yang and B. Xian, "Energy-based nonlinear adaptive control design for the quadrotor UAV system with a suspended payload," *IEEE Trans. Ind. Electron.*, vol. 67, no. 3, pp. 2054–2064, Mar. 2020.
- [4] P. Kumar, I. Bensekrane, and R. Merzouki, "Power consumption modeling of wheeled mobile robots with multiple driving modes," *IEEE Trans. Ind. Electron.*, vol. 70, no. 10, pp. 10282–10291, Oct. 2023.
- [5] L. Chen, R. Cui, C. Yang, and W. Yan, "Adaptive neural network control of underactuated surface vessels with guaranteed transient performance: Theory and experimental results," *IEEE Trans. Ind. Electron.*, vol. 67, no. 5, pp. 4024–4035, May 2020.
- [6] M. Xu, A. Hu, and H. Wang, "Image-based visual impedance force control for contact aerial manipulation," *IEEE Trans. Autom. Sci. Eng.*, vol. 20, no. 1, pp. 518–527, Jan. 2023.
- [7] B. Xian and S. Yang, "Robust tracking control of a quadrotor unmanned aerial vehicle-suspended payload system," *IEEE/ASME Trans. Mechatron.*, vol. 26, no. 5, pp. 2653–2663, Oct. 2021.
- [8] G. Yu, D. Cabecinhas, R. Cunha, and C. Silvestre, "Aggressive maneuvers for a quadrotor-slung-load system through fast trajectory generation and tracking," *Auton. Robots*, vol. 46, no. 4, pp. 499–513, 2022.
- [9] A. Akhtar, S. Saleem, and J. Shan, "Path following of a quadrotor with a cable-suspended payload," *IEEE Trans. Ind. Electron.*, vol. 70, no. 2, pp. 1646–1654, Feb. 2023.
- [10] X. Liang, Y. Fang, N. Sun, H. Lin, and X. Zhao, "Adaptive nonlinear hierarchical control for a rotorcraft transporting a cable-suspended payload," *IEEE Trans. Syst., Man, Cybern. Syst.*, vol. 51, no. 7, pp. 4171–4182, Jul. 2021.

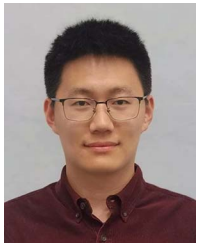
- [11] B. Jiang, K. Zhang, C. Liu, and H. Yang, "Fault diagnosis and accommodation with flight control applications," *J. Control Decis.*, vol. 7, no. 1, pp. 24–43, 2020.
- [12] R. C. Avram, X. Zhang, and J. Muse, "Nonlinear adaptive fault-tolerant quadrotor altitude and attitude tracking with multiple actuator faults," *IEEE Trans. Control Syst. Technol.*, vol. 26, no. 2, pp. 701–707, Mar. 2018.
- [13] S. Mallavalli and A. Fekih, "A fault tolerant control design for actuator fault mitigation in quadrotor UAVs," in *Proc. Amer. Control Conf.*, 2019, pp. 5111–5116.
- [14] Y. Song, L. He, D. Zhang, J. Qian, and J. Fu, "Neuroadaptive fault-tolerant control of quadrotor UAVs: A more affordable solution," *IEEE Trans. Neural Netw. Learn. Syst.*, vol. 30, no. 7, pp. 1975–1983, Jul. 2019.
- [15] Z. Hou, P. Lu, and Z. Tu, "Nonsingular terminal sliding mode control for a quadrotor UAV with a total rotor failure," *Aerosp. Sci. Technol.*, vol. 98, 2020, Art. no. 105716.
- [16] W. Chung and H. Son, "Fault-tolerant control of multirotor UAVs by control variable elimination," *IEEE/ASME Trans. Mechatron.*, vol. 25, no. 5, pp. 2513–2522, Oct. 2020.
- [17] B. Wang, Y. Shen, and Y. Zhang, "Active fault-tolerant control for a quadrotor helicopter against actuator faults and model uncertainties," *Aerosp. Sci. Technol.*, vol. 99, 2020, Art. no. 105745.
- [18] C. Ke, K.-Y. Cai, and Q. Quan, "Uniform fault-tolerant control of a quadcopter with rotor failure," *IEEE/ASME Trans. Mechatron.*, vol. 28, no. 1, pp. 507–517, Feb. 2023.
- [19] M. Qian, Z. Zhang, Z. Zheng, and C. Bo, "Sliding mode control-based distributed fault tolerant tracking control for multiple unmanned aerial vehicles with input constraints and actuator faults," *Int. J. Robust Nonlinear Control*, vol. 33, pp. 9150–9173, 2022.
- [20] K. Ahmadi, D. Asadi, A. Merheb, S.-Y. Nabavi-Chashmi, and O. Tutsoy, "Active fault-tolerant control of quadrotor UAVs with nonlinear observer-based sliding mode control validated through hardware in the loop experiments," *Control Eng. Pract.*, vol. 137, 2023, Art. no. 105557.
- [21] M. Zhang and X. Jing, "Model-free saturated PD-SMC method for 4-DOF tower crane systems," *IEEE Trans. Ind. Electron.*, vol. 69, no. 10, pp. 10270–10280, Oct. 2022.
- [22] B. Zhao, H. Ouyang, and M. Iwasaki, "Motion trajectory tracking and sway reduction for double-pendulum overhead cranes using improved adaptive control without velocity feedback," *IEEE/ASME Trans. Mechatron.*, vol. 27, no. 5, pp. 3648–3659, Oct. 2022.
- [23] K. Sreenath, T. Lee, and V. Kumar, "Geometric control and differential flatness of a quadrotor UAV with a cable-suspended load," in *Proc. 52nd IEEE Conf. Decis. Control*, 2013, pp. 2269–2274.
- [24] Z.-Y. Lv, Y. Wu, and W. Rui, "Nonlinear motion control for a quadrotor transporting a cable-suspended payload," *IEEE Trans. Veh. Technol.*, vol. 69, no. 8, pp. 8192–8206, Aug. 2020.
- [25] D. Hashemi and H. Heidari, "Trajectory planning of quadrotor UAV with maximum payload and minimum oscillation of suspended load using optimal control," *J. Intell. Robot. Syst.*, vol. 100, no. 3/4, pp. 1369–1381, 2020.
- [26] X. Liang, Y. Fang, N. Sun, and H. Lin, "Dynamics analysis and time-optimal motion planning for unmanned quadrotor transportation systems," *Mechatronics*, vol. 50, pp. 16–29, 2018.
- [27] G. J. Leishman, *Principles of Helicopter Aerodynamics With CD Extra*. Cambridge, U.K.: Cambridge Univ. Press, 2006.
- [28] K. Guo, W. Zhang, Y. Zhu, J. Jia, X. Yu, and Y. Zhang, "Safety control for quadrotor UAV against ground effect and blade damage," *IEEE Trans. Ind. Electron.*, vol. 69, no. 12, pp. 13373–13383, Dec. 2022.
- [29] X. Wang, S. Sun, E.-J. van Kampen, and Q. Chu, "Quadrotor fault tolerant incremental sliding mode control driven by sliding mode disturbance observers," *Aerosp. Sci. Technol.*, vol. 87, pp. 417–430, 2019.
- [30] B. Wang, X. Yu, L. Mu, and Y. Zhang, "Disturbance observer-based adaptive fault-tolerant control for a quadrotor helicopter subject to parametric uncertainties and external disturbances," *Mech. Syst. Signal Process.*, vol. 120, pp. 727–743, 2019.
- [31] X. Wu, Y. Zhao, and K. Xu, "Nonlinear disturbance observer based sliding mode control for a benchmark system with uncertain disturbances," *ISA Trans.*, vol. 110, pp. 63–70, 2021.
- [32] T. Lee, M. Leok, and N. H. McClamroch, "Geometric tracking control of a quadrotor UAV on SE(3)," in *Proc. IEEE 49th Conf. Decis. Control*, 2010, pp. 5420–5425.
- [33] D. Jiang, G. Wen, Z. Peng, J.-L. Wang, and T. Huang, "Fully distributed pull-based event-triggered bipartite fixed-time output control of heterogeneous systems with an active leader," *IEEE Trans. Cybern.*, vol. 53, no. 5, pp. 3089–3100, May 2023.
- [34] Z. Zuo and L. Tie, "Distributed robust finite-time nonlinear consensus protocols for multi-agent systems," *Int. J. Syst. Sci.*, vol. 47, no. 6, pp. 1366–1375, 2016.
- [35] Y. Yang, L. Tang, W. Zou, J. Guo, and C. K. Ahn, "Dynamic event-triggered design with fixed-time performance and input dead-zone," *IEEE Trans. Circuits Syst. II, Exp. Briefs*, vol. 69, no. 11, pp. 4344–4348, Nov. 2022.
- [36] T. Lee, "Robust adaptive attitude tracking on SO(3) with an application to a quadrotor UAV," *IEEE Trans. Control Syst. Technol.*, vol. 21, no. 5, pp. 1924–1930, Sep. 2012.
- [37] F. A. Goodarzi, D. Lee, and T. Lee, "Geometric adaptive tracking control of a quadrotor unmanned aerial vehicle on SE(3) for agile maneuvers," *J. Dyn. Syst., Meas., Control*, vol. 137, no. 9, 2015, Art. no. 091007.
- [38] S. Li, J. Yang, W.-H. Chen, and X. Chen, *Disturbance Observer-Based Control: Methods and Applications*. Boca Raton, FL, USA: CRC Press, 2014.
- [39] C. Ott, *Cartesian Impedance Control of Redundant and Flexible-Joint Robots*. Berlin, Germany: Springer, 2008.
- [40] G. Yu, D. Cabecinhas, R. Cunha, and C. Silvestre, "Nonlinear backstepping control of a quadrotor-slung load system," *IEEE/ASME Trans. Mechatron.*, vol. 24, no. 5, pp. 2304–2315, Oct. 2019.
- [41] F. Kendoul, "Nonlinear hierarchical flight controller for unmanned rotorcraft: Design, stability, and experiments," *J. Guid., Control, Dyn.*, vol. 32, no. 6, pp. 1954–1958, 2009.
- [42] B. Zhao, B. Xian, Y. Zhang, and X. Zhang, "Nonlinear robust adaptive tracking control of a quadrotor UAV via immersion and invariance methodology," *IEEE Trans. Ind. Electron.*, vol. 62, no. 5, pp. 2891–2902, May 2015.
- [43] S. Wang, J. Chen, and X. He, "An adaptive composite disturbance rejection for attitude control of the agricultural quadrotor UAV," *ISA Trans.*, vol. 129, pp. 564–579, 2022.
- [44] B. Ghalamchi, Z. Jia, and M. W. Mueller, "Real-time vibration-based propeller fault diagnosis for multicopters," *IEEE/ASME Trans. Mechatron.*, vol. 25, no. 1, pp. 395–405, Feb. 2020.
- [45] C. Song, C. Wei, F. Yang, and N. Cui, "High-order sliding mode-based fixed-time active disturbance rejection control for quadrotor attitude system," *Electronics*, vol. 7, no. 12, 2018, Art. no. 357.
- [46] R. Puchalski, A. Bondyra, W. Giernacki, and Y. Zhang, "Actuator fault detection and isolation system for multirotor unmanned aerial vehicles," in *Proc. 26th Int. Conf. Methods Models Autom. Robot.*, 2022, pp. 364–369.
- [47] Z. Lv, Y. Wu, X.-M. Sun, and Q.-G. Wang, "Fixed-time control for a quadrotor with a cable-suspended load," *IEEE Trans. Intell. Transp. Syst.*, vol. 23, no. 11, pp. 21932–21943, Nov. 2022.
- [48] T.-I. Yeom and D.-C. Lee, "Design of sliding-mode speed controller with active damping control for single-inverter dual-PMSM drive systems," *IEEE Trans. Power Electron.*, vol. 36, no. 5, pp. 5794–5801, May 2021.
- [49] J. Hu, Q. Sun, R. Wang, B. Wang, M. Zhai, and H. Zhang, "Privacy-preserving sliding mode control for voltage restoration of AC microgrids based on output mask approach," *IEEE Trans. Ind. Inform.*, vol. 18, no. 10, pp. 6818–6827, Oct. 2022.
- [50] Z. Echreshavi, M. Farbood, and M. Shasadeghi, "Fuzzy event-triggered integral sliding mode control of nonlinear continuous-time systems," *IEEE Trans. Fuzzy Syst.*, vol. 30, no. 7, pp. 2347–2359, Jul. 2022.
- [51] D. Yang, T. Li, X. Xie, and H. Zhang, "Event-triggered integral sliding-mode control for nonlinear constrained-input systems with disturbances via adaptive dynamic programming," *IEEE Trans. Syst., Man, Cybern. Syst.*, vol. 50, no. 11, pp. 4086–4096, Nov. 2020.
- [52] C. Wu, A. van der Schaft, and J. Chen, "Robust trajectory tracking for incrementally passive nonlinear systems," *Automatica*, vol. 107, pp. 595–599, 2019.
- [53] Z. Xing, Y. Zhang, and C.-Y. Su, "Active wind rejection control for a quadrotor UAV against unknown winds," *IEEE Trans. Aerosp. Electron. Syst.*, vol. 59, no. 6, pp. 8956–8968, Dec. 2023.
- [54] R. R. Nair, L. Behera, and S. Kumar, "Event-triggered finite-time integral sliding mode controller for consensus-based formation of multirobot systems with disturbances," *IEEE Trans. Control Syst. Technol.*, vol. 27, no. 1, pp. 39–47, Jan. 2019.
- [55] S. Ahmed, H. Wang, and Y. Tian, "Adaptive high-order terminal sliding mode control based on time delay estimation for the robotic manipulators with backlash hysteresis," *IEEE Trans. Syst., Man, Cybern. Syst.*, vol. 51, no. 2, pp. 1128–1137, Feb. 2021.
- [56] X. Sun, Y. Xiong, J. Yang, and X. Tian, "Torque ripple reduction for a 12/8 switched reluctance motor based on a novel sliding mode control strategy," *IEEE Trans. Transport. Electric.*, vol. 9, no. 1, pp. 359–369, Mar. 2023.

- [57] S. Xie, Q. Chen, and Q. Yang, "Adaptive fuzzy predefined-time dynamic surface control for attitude tracking of spacecraft with state constraints," *IEEE Trans. Fuzzy Syst.*, vol. 31, no. 7, pp. 2292–2304, Jul. 2023.
- [58] M. Labbadi and M. Cherkaoui, "Robust adaptive nonsingular fast terminal sliding-mode tracking control for an uncertain quadrotor UAV subjected to disturbances," *ISA Trans.*, vol. 99, pp. 290–304, 2020.
- [59] N. Harl and S. N. Balakrishnan, "Impact time and angle guidance with sliding mode control," *IEEE Trans. Control Syst. Technol.*, vol. 20, no. 6, pp. 1436–1449, Nov. 2012.
- [60] A. M. Parrany and A. Alasty, "Decentralized aggregation and leader-following control of a swarm of quadcopters with nonlinear under-actuated dynamics," *Aerosp. Sci. Technol.*, vol. 107, 2020, Art. no. 106317.



Hai Yu (Graduate Student, Member) received the B.S. degree in automation from Jilin University, Changchun, China, in 2020. He is currently working toward the Ph.D. degree in control science and engineering with the Institute of Robotics and Automatic Information System, Nankai University, Tianjin, China.

His research interests include nonlinear control of unmanned aerial vehicles.



Shizhen Wu (Graduate Student Member, IEEE) received the B.S. degree in information and computing science from the School of Mathematics, Hefei University of Technology, Hefei, China, in 2019. He is currently working toward the Ph.D. degree in control science and engineering with the Institute of Robotics and Automatic Information System, Nankai University, Tianjin, China.

His research interests include hybrid dynamics and control, safety verification, and coordination of multiple underactuated robotics.



Wei He received the B.S. degree in intelligent science and technology, in 2019, from Nankai University, Tianjin, China, where he is currently working toward the Ph.D. degree in control science and engineering with the Institute of Robotics and Automatic Information System.

His research interests include motion planning, state estimation and intelligent control of robots, especially unmanned aerial vehicles and aerial manipulation systems.



Xiao Liang (Member, IEEE) received the B.S. degree in intelligence science and technology from the Hebei University of Technology, Tianjin, China, in 2013, and the Ph.D. degree in control theory and control engineering from Nankai University, Tianjin, in 2018.

He is currently an Associate Professor with the Institute of Robotics and Automatic Information System, Nankai University. His research interests include motion planning and nonlinear control of unmanned aerial vehicle systems.



Jianda Han (Member, IEEE) received the Ph.D. degree in mechatronics engineering from the Harbin Institute of Technology, Harbin, China, in 1998.

He is currently a Professor with the Institute of Robotics and Automatic Information System, Nankai University, Tianjin, China. From 1998 to 2003, he was a Visiting Scientist with the City University of Hong Kong, Hong Kong; Michigan State University, East Lansing, MI, USA; and Cornell University, Ithaca, NY, USA. His research interests include nonlinear estimation and control, robotics, and mechatronics systems.

search interests include nonlinear estimation and control, robotics, and mechatronics systems.



Yongchun Fang (Senior Member, IEEE) received the B.S. and M.S. degrees in control theory and applications from Zhejiang University, Hangzhou, China, in 1996 and 1999, respectively, and the Ph.D. degree in electrical engineering from Clemson University, Clemson, SC, USA, in 2002.

He is currently a Professor with the Institute of Robotics and Automatic Information System, Nankai University, Tianjin, China. From 2002 to 2003, he was a Postdoctoral Fellow with the Sibley School of Mechanical and Aerospace Engineering, Cornell University, Ithaca, NY, USA. His research interests include nonlinear control, visual servoing, control of underactuated systems, and atomic force microscopy (AFM)-based nanosystems.

Dr. Fang was the recipient of the National Science Fund for Distinguished Young Scholars of China. He was an Associate Editor for the *ASME Journal of Dynamic Systems, Measurement, and Control*.